



# Elucidating the role of $\text{La}^{3+}/\text{Sm}^{3+}$ in the carbon paths of dry reforming of methane over Ni/Ce-La(Sm)-Cu-O using transient kinetics and isotopic techniques



Aseel G.S. Hussien <sup>a,b,1</sup>, Constantinos M. Damaskinos <sup>c,1</sup>, Aasif A. Dabbawala <sup>a,b</sup>, Dalaver H. Anjum <sup>b,d</sup>, Michalis A. Vasiliades <sup>c</sup>, Maryam T.A. Khaleel <sup>b,e</sup>, Nimer Wehbe <sup>f</sup>, Angelos M. Efstathiou <sup>c,\*</sup>, Kyriaki Polychronopoulou <sup>a,b,\*\*</sup>

<sup>a</sup> Department of Mechanical Engineering, Khalifa University of Science and Technology, Main Campus, P.O. Box 127788, Abu Dhabi, United Arab Emirates

<sup>b</sup> Center for Catalysis and Separations, Khalifa University of Science and Technology, P.O. Box 127788, Abu Dhabi, United Arab Emirates

<sup>c</sup> Department of Chemistry, Heterogeneous Catalysis Laboratory, University of Cyprus, 1 University Ave., University Campus, 2109 Nicosia, Cyprus

<sup>d</sup> Department of Physics, Khalifa University of Science and Technology, Main Campus, P.O. Box 127788, Abu Dhabi, United Arab Emirates

<sup>e</sup> Department of Chemical Engineering, Khalifa University, P.O. Box 127788, Abu Dhabi, United Arab Emirates

<sup>f</sup> Core Labs, King Abdullah University of Science and Technology (KAUST), Thuwal 23955-6900, Saudi Arabia

## ARTICLE INFO

### Keywords:

Doped ceria

Supported Ni catalysts

DRM

Coking

Lattice oxygen

Transient isotopic techniques

## ABSTRACT

The different effects of the presence of  $\text{La}^{3+}$  and  $\text{Sm}^{3+}$  heteroatoms in the 5 wt% Ni/45Ce-45(Sm or La)-10Cu-O catalytic system on the carbon deposition and removal reaction paths in the dry reforming of methane (DRM) at 750 °C were investigated using transient kinetic and isotopic experiments. The relative initial rates of carbon oxidation by lattice oxygen of support and that by oxygen derived from  $\text{CO}_2$  dissociation under DRM reaction conditions were quantified. Ni nanoparticles (23-nm) supported on La  $^{3+}$ -doped ceria exhibited at least 3 times higher initial rates of carbon oxidation to CO by lattice oxygen, and ~ 13 times lower rates of carbon accumulation than Ni (18-nm) supported on Sm  $^{3+}$ -doped ceria. The concentration and mobility of labile surface oxygen at the Ni-support interface region seems to correlate with carbon accumulation. Ni/Ce-La(or Sm)-10Cu-O formed NiCu alloy nanoparticles, partly responsible for lowering carbon deposition and increasing carbon oxidation rates to CO.

## 1. Introduction

The interest in dry reforming of methane (DRM) catalytic process ( $\text{CH}_4 + \text{CO}_2 \leftrightarrow 2 \text{CO} + 2 \text{H}_2$ ;  $\Delta H^\circ = + 247.3 \text{ kJ mol}^{-1}$ ) is driven by the fact that clean and green H<sub>2</sub> fuel and synthesis gas (CO/H<sub>2</sub>) can be produced, the latter being used for the production of fuels and high value-added chemicals such as methanol, dimethyl ether and acetic acid [1–7]. At the same time, advances in CO<sub>2</sub> capture technologies and their utilization in DRM mitigates global warming [8–10]. In spite of the practical importance of DRM, this has not been industrialized yet due to the lack of development of robust catalysts that can sustain coke-free operation and high resistance to metal sintering at the required

temperatures (ca. > 700 °C) [2,11,12].

The economic feasibility of using Ni-based catalysts than noble metal (Pt, Rh, Ru and Ir)-based counterparts presents nowadays a viable solution for the development of DRM [2,11]. Nickel metal supported catalysts, however, suffer mainly from carbon deposition, which ultimately leads to catalyst deactivation. Carbon deposition and accumulation under DRM mainly originates from CH<sub>4</sub> decomposition (Eq. (1)) and CO disproportionation reactions (reverse Boudouard, Eq. (2)), which could occur simultaneously with different rates under DRM reaction conditions [11–17]. CH<sub>4</sub> decomposition produces active carbon which is oxidized to CO gas product by atomic oxygen via the CO<sub>2</sub> activation route but also by labile oxygen when highly reducible

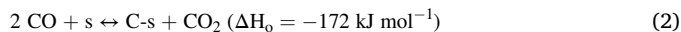
\* Corresponding author.

\*\* Corresponding author at: Department of Mechanical Engineering, Khalifa University of Science and Technology, Main Campus, P.O. Box 127788, Abu Dhabi, United Arab Emirates.

E-mail addresses: [efstath@ucy.ac.cy](mailto:efstath@ucy.ac.cy) (A.M. Efstathiou), [kyriaki.polychrono@ku.ac.ae](mailto:kyriaki.polychrono@ku.ac.ae) (K. Polychronopoulou).

<sup>1</sup> Equal contribution.

supports are used. The importance of the latter process was recently demonstrated by advanced transient isotopic experiments [15–22]. Inactive carbon in the form of fibers, whiskers, and graphite, is the result of polymerization of part of the carbon formed mainly by CH<sub>4</sub> decomposition.



The fact that the support's lattice oxygen could play a major role in tackling the coking problem [2,16,19,21,23], Ni supported on *doped ceria carriers* have been studied in addition to many other Ni-based catalytic systems, due to their remarkable coke resistance performance [17,21–26]. This was attributed to ceria's ability to switch easily between Ce<sup>+4</sup> and Ce<sup>+3</sup> oxidation states and release lattice oxygen, O<sub>o</sub> with the subsequent formation of oxygen vacancies, V<sub>o</sub> (Eq. (3), use of Kröger and Vink defect notation) [27]. Oxygen vacant sites promote CO<sub>2</sub> dissociation (Eq. (4)) with the subsequent gasification of carbon species by lattice oxygen on the catalyst surface (Eq. (5)) [15,20,22,28,29].



CeO<sub>2</sub> has been largely used in a wide range of catalytic applications since the 1950s mainly because of its redox properties [27]. Studies on doped ceria solids showed that *trivalent heteroatoms* such as La<sup>3+</sup>, Sm<sup>3+</sup> and Pr<sup>3+</sup> improve significantly their lattice oxygen mobility [30,31]. Bernal et al. [32], Polychronopoulou et al. [33], and Makri et al. [16] found that the basicity of ceria support increases with La<sup>+3</sup>- and Pr<sup>+3</sup>-doping, which was usually related to the enhancement of catalyst's carbon resistance in hydrocarbon reforming processes. Kambolis et al. [34] reported that the increase in oxygen storage capacity (OSC) of Ni/CeO<sub>2</sub>-ZrO<sub>2</sub> improved the DRM catalytic activity when compared to Ni/CeO<sub>2</sub> or Ni/ZrO<sub>2</sub> but without finding a certain relationship with the Ce:Zr ratio and carbon deposition rate, as opposed to the works of Kumar et al. [35] and Wolfbeisser et al. [36] who reported that carbon deposition rate was decreased over Ni supported on CeO<sub>2</sub>-ZrO<sub>2</sub> than pure CeO<sub>2</sub> or ZrO<sub>2</sub> carrier.

Fundamental understanding of the effect of the chemical nature of rare-earth metal heteroatoms in CeO<sub>2</sub> when used as carriers of Ni on the DRM activity and carbon deposition rate over doped ceria-supported Ni appears limited. Pino et al. [37] investigated the 3.7 wt% Ni/CeO<sub>2</sub>-La<sub>2</sub>O<sub>3</sub> (Ce<sub>0.70</sub>La<sub>0.20</sub>Ni<sub>0.10</sub>O<sub>2-δ</sub>) catalytic system focusing on the metal-support interactions and the effect of surface basicity. The authors showed that the presence of La<sub>2</sub>O<sub>3</sub> led to carbon gasification and CO<sub>2</sub> enhanced chemisorption, factors responsible for an improved catalyst activity and stability with respect to Ni/CeO<sub>2</sub>. Luisetto et al. [24] examined the role of heteroatoms (M = Sm, La, Zr) in CeO<sub>2</sub> for the CO<sub>2</sub> activation route in the DRM. In the case of Ni/Ce<sub>0.85</sub>M<sub>0.15</sub>O<sub>2-δ</sub> catalysts, the aliovalent Sm<sup>3+</sup> and La<sup>3+</sup> cations decreased the carbon formation rate by improving surface basicity. Vasiliades et al. [22] investigated the effect of Ce/Pr ratio on the carbon pathways in the DRM at 750 °C over a series of 5 wt% Ni/Ce<sub>1-x</sub>Pr<sub>x</sub>O<sub>2-δ</sub> catalysts of similar mean Ni particle size. A remarkable drop in carbon deposition rate was measured when 20 at% Ce was replaced for 20 at% Pr in the Ce-Pr-O matrix (solid solution) with only a small drop in activity.

The effect of La<sup>3+</sup> and Sm<sup>3+</sup> doping on the formation and ordering of oxygen vacancies in doped ceria was reported [38–42]. Studies have shown that the reactivity of co-doped ceria materials is influenced by numerous parameters, such as electronic configuration, coordination, oxidation state, heteroatom cation size, and interactions between heteroatom-vacancy and vacancy-vacancy [43,44]. Doping the ceria lattice with larger or smaller in size cations than Ce<sup>+4</sup> will result in the formation of vacancy-Ce<sup>+4</sup> or vacancy-heteroatom sites, respectively,

changing the local environment and lattice strain [45,46].

The preparation method used to synthesize doped ceria materials greatly affects also the DRM reaction performance, as it controls the compositional homogeneity of the formed solid solution and its nano-structure, thus affecting its redox properties [29,47,48]. For instance, Damaskinos et al. [29] reported on DRM over Ni/CeO<sub>2</sub> prepared by different methods: thermal decomposition, precipitation, hydrothermal, and sol-gel. The authors probed using transient techniques a profound effect of the synthesis method on the carbon paths of CH<sub>4</sub> activation and CO disproportionation. The precipitation method led to a catalyst with the lowest amount of carbon accumulation amongst the investigated series of catalysts. Various methods are used to synthesize doped ceria materials, namely: hydrothermal, sol-gel, combustion, solvothermal, spray pyrolysis, precipitation and microwave [47,49–51]. The latter method enhances the rates of chemical reactions during synthesis [52,53].

Introduction of Cu into the ceria lattice was previously shown by us to largely enhance oxygen mobility in co-doped CeO<sub>2-x</sub> with both La-Cu [40], and Sm-Cu [41]. In the present work the effect of La or Sm introduction in the Ce-10Cu-O (Ce:Cu = 9:1 atom ratio) lattice (via enhanced microwave synthesis) on the activity and carbon paths of DRM over 5 wt% Ni/Ce-40La (or Sm)-10Cu-O catalysts was investigated. The emphasis of this work, where its novelty lies in, is the use of advanced transient kinetic and isotopic (use of <sup>18</sup>O<sub>2</sub>) experiments to understand the influence of La<sup>3+</sup> vs. Sm<sup>3+</sup> co-dopants on important issues of the DRM reaction, namely: (i) the relative contribution of methane decomposition and CO disproportionation routes in carbon formation, (ii) the rate of carbon accumulating during DRM (up to 100 h), and (iii) the extent of participation of support's labile oxygen in the removal of carbon from the catalyst surface via oxidation to CO. Various spectroscopic and other characterization techniques (XRD, HRTEM, Raman, H<sub>2</sub>-TPR, CO<sub>2</sub>-TPD and H<sub>2</sub>-TPD) were employed to gather information on the effect of La<sup>3+</sup> and Sm<sup>3+</sup> heteroatoms in several intrinsic properties of doped/ promoted ceria-supported Ni catalysts, e.g., crystallinity/microstructure, morphology, surface basicity and redox behavior, and their relationships with DRM and transient kinetics performance.

## 2. Experimental

### 2.1. Synthesis of doped/promoted ceria supports

The ternary oxide supports of 10 at% Cu content were synthesized via an enhanced microwave approach. Each metal precursor, Ce (NO<sub>3</sub>)<sub>3</sub>·6H<sub>2</sub>O (99.95%), La(NO<sub>3</sub>)<sub>3</sub>·6H<sub>2</sub>O (99.95%) and Cu(NO<sub>3</sub>)<sub>2</sub>·3H<sub>2</sub>O (99.95%) (Sigma-Aldrich, USA), was dissolved in distilled water with the appropriate molar ratio so as to obtain Ce and Sm or La of 45 at% content. In the case of Ce-Sm-Cu-O, Ce(NO<sub>3</sub>)<sub>3</sub>·6H<sub>2</sub>O (99.95%), Sm (NO<sub>3</sub>)<sub>3</sub>·6H<sub>2</sub>O (99.95%) and Cu(NO<sub>3</sub>)<sub>2</sub>·3H<sub>2</sub>O (99.95%) metal precursors (Sigma-Aldrich, USA) were used. The total metal loading was kept at 0.03 mol in both synthesis solutions of the solids. The complexing agent (ethylene glycol) was dissolved in distilled water, while maintaining a 2:1 (v/v) ratio of ethylene glycol to distilled water. The metal solution and the ethylene glycol were mixed and exposed to microwave heating at 130 and 170 °C, while continuous stirring was applied. The solution was then centrifuged, and the obtained solid was calcined in air at 500 °C for 6 h. The thus obtained solid supports were coded as Ce-Sm-10Cu-O and Ce-La-10Cu-O.

### 2.2. Synthesis of supported Ni catalysts

The supported Ni catalysts where prepared by the wet impregnation method using Ni(NO<sub>3</sub>)<sub>2</sub>·6H<sub>2</sub>O (Aldrich) as nickel metal precursor. A given amount of precursor solution (distilled de-ionized water was used as solvent) corresponding to a nominal Ni loading of 5 wt% was used to impregnate the metal oxide (in powder form) at 50 °C. After impregnation and drying overnight at 120 °C, the obtained solid was calcined in

air at 500 °C/2 h and stored for further use. Prior to any catalytic tests, the supported Ni catalyst sample was recalcined at 750 °C/2 h (static air, furnace) and then in situ reduced in H<sub>2</sub> at 750 °C/2 h (fresh catalyst).

### 2.3. Characterization of catalysts

#### 2.3.1. Powder X-ray diffraction (PXRD)

Powder XRD analysis was conducted over the as prepared supported Ni catalysts (Section 2.2) calcined at 750 °C/2 h (without H<sub>2</sub> reduction) by using a Shimadzu 6000 Series diffractometer (CuKa radiation,  $\lambda = 0.15418$  nm). X-ray diffractograms were recorded in the 2 $\theta$  range of 20–80°, with a scan speed of 2° min<sup>-1</sup>, an increment of 0.02°, and a dwell time of 0.6 s. The lattice parameter ( $a$ , Å) and the mean primary crystallite size ( $d_c$ , nm) of the support's single-phase solid solution (ceria pseudo-cubic structure), and that of NiO phase, were estimated using the Scherrer equation [54]. Conversion of the  $d_{\text{NiO}}$  to  $d_{\text{Ni}}$  (nm) was made after assuming same crystallite geometrical shape for Ni and NiO and using the mass densities of Ni and NiO bulk phases, according to Eq. (6):

$$d(\text{Ni, nm}) = d(\text{NiO, nm}) \times 0.847 \quad (6)$$

#### 2.3.2. Electron microscopy: High resolution transmission electron microscopy (HR-TEM) and scanning electron microscopy (SEM)

HR-TEM studies were conducted over the fresh supported Ni catalysts as well as the best performed Ni catalyst (following 100 h of DRM reaction) with the use of an electron microscope (model Titan 80-300 ST) operated at 300 kV. The microscope was equipped with a spherical aberration (Cs) corrector for the image (CEOS CETCOR), and an energy filter (model GIF Quantum 963, Gatan, Inc.). Selected powdered specimens were dispersed in ethanol and drop casted onto carbon-coated copper grid (200 mesh) to perform imaging, structure, and composition elemental mapping analyses. The high-resolution imaging was performed in aberration corrected TEM mode, while the structure analysis was carried out using the selected area electron diffraction (SAED) technique. The composition of samples was determined after using X-ray energy dispersive (EDX) spectroscopy. Nanoscale elemental mapping was carried out after using electron energy loss spectroscopy (EELS), in conjunction with the STEM mode. The entire TEM data acquisition and post processing was performed by utilizing Gatan Microscopy Suite (GMS) software (version 3.2).

The materials morphology and composition were assessed using Scanning Electron Microscopy coupled with Energy Dispersive X-ray Spectroscopy (Quanta 250 ESEM). The samples were prepared on aluminum stubs, mounted using carbon tapes, followed by sputter coating with a 7.5-nm layer of palladium (Pd). The composition values reported were the average values based on measurements at five different sample areas.

#### 2.3.3. Raman spectroscopy

Raman spectroscopy was performed to complement powder XRD and probe the oxygen sublattice and induced structural defects. A Raman–AFM combination (Witec Alpha 300 RA, Ulm, Germany) with a laser wavelength of 532 nm (green laser) were used.

#### 2.3.4. Textural analysis of solids

A 3Flex physisorption porosimeter (Micrometrics, Atlanta, GA, USA) was used to acquire N<sub>2</sub> adsorption-desorption isotherms at 77 K of the supported Ni catalysts calcined at 750 °C/2 h. The catalysts were first degassed at 150 °C (overnight) before any measurements. The Brunauer–Emmett–Teller (BET) method [55] was used to estimate the specific surface area (SSA, m<sup>2</sup> g<sup>-1</sup>), while the Barrett–Joyner–Halenda (BJH)

method [56] was used to estimate the pore size distribution of the supported Ni catalysts.

#### 2.3.5. H<sub>2</sub> temperature-programmed reduction (H<sub>2</sub>-TPR)

H<sub>2</sub>-TPR experiments were performed on a gas-flow system for transient kinetic studies previously described [21,22]. Initially, 20% O<sub>2</sub>/He gas mixture was passed over the catalyst (W = 0.1 g) while ramping the temperature to 700 °C at the rate of 30 °C/min, and the catalyst sample was kept at 700 °C for 15 min. The gas was then switched to He for 10 min, and the catalyst was cooled down to 35 °C (30 °C/min) in He gas flow. The temperature of the solid was then increased to 700 °C at the rate of 30 °C/min in 5.18 vol% H<sub>2</sub>/Ar gas atmosphere (50 NmL min<sup>-1</sup>). The H<sub>2</sub> signal ( $m/z = 2$ ) was recorded by online mass spectrometer (Balzers, Omnistar 1-200 amu), and it was converted to mol% after using a certified H<sub>2</sub> gas mixture. The appropriate material balance was used to report H<sub>2</sub>-TPR traces in terms of reduction rate (μmol H<sub>2</sub> g<sub>cat</sub><sup>-1</sup> s<sup>-1</sup>) vs temperature. Integration of the H<sub>2</sub>-TPR trace provided the amount of H<sub>2</sub> consumed (μmol H<sub>2</sub> g<sub>cat</sub><sup>-1</sup>) or oxygen removed from the solid (μmol O g<sub>cat</sub><sup>-1</sup>).

#### 2.3.6. CO<sub>2</sub> temperature-programmed desorption (TPD)

CO<sub>2</sub> temperature-programmed desorption (CO<sub>2</sub>-TPD) experiments were conducted to characterize the surface basic sites of the supported Ni catalysts. The as prepared catalyst sample (Section 2.2) before loaded in the microreactor was calcined at 750 °C/2 h (static air, furnace). It was then placed in the micro-reactor (W = 0.1 g) and the sample temperature was increased to 750 °C at the rate of 30 °C/min in the flow of 20% O<sub>2</sub>/He and kept for 30 min. The feed gas was then switched to He (10 min at 750 °C) and the catalyst sample was then cooled to 30 °C. Adsorption of carbon dioxide was conducted at 30 °C from a 5 vol% CO<sub>2</sub>/He gas mixture until saturation of the basic sites of the solid; no further CO<sub>2</sub> consumption was noticed by monitoring the CO<sub>2</sub> signal ( $m/z = 44$ ) in the mass spectrometer. The feed gas was then switched to He (30 NmL min<sup>-1</sup>) and an increase of the catalyst temperature to 700 °C (ramp at 30 °C/min) was made, while the evolution of gaseous CO<sub>2</sub> from the reactor was continuously monitored by online mass spectrometry. The CO<sub>2</sub> signal was converted into mole fraction after calibration, and the CO<sub>2</sub>-TPD trace is presented as desorption rate (μmol CO<sub>2</sub> g<sub>cat</sub><sup>-1</sup> s<sup>-1</sup>) versus temperature. Integration of the CO<sub>2</sub>-TPD trace and using the appropriate material balance provided the amount of CO<sub>2</sub> adsorbed (μmol CO<sub>2</sub> g<sub>cat</sub><sup>-1</sup>). After considering the BET area of the catalyst sample, the density of basic sites (μmol CO<sub>2</sub> m<sup>-2</sup>) was estimated.

#### 2.3.7. Hydrogen temperature-programmed desorption (H<sub>2</sub>-TPD)

The H<sub>2</sub>-TPD technique was used to investigate the hydrogen adsorption states over the supported Ni catalysts. The catalyst sample before loaded in the microreactor was calcined at 750 °C/4 h (static air, furnace). Then, 0.1 g of sample was loaded in the reactor, and the temperature was increased in He gas flow to 750 °C. The sample was then reduced in hydrogen gas flow (1 bar) at 750 °C/2 h, followed by He purge at 750 °C until the H<sub>2</sub>-mass spectrometer signal reached its background value. The catalyst was then cooled quickly to 30 °C in He flow followed by 30-min exposure to a 0.5 vol% H<sub>2</sub>/He adsorption gas. H-spillover was avoided under these chemisorption conditions; use of lower or higher adsorption times in H<sub>2</sub>/He resulted in very similar chemisorption amounts (within experimental error). After H<sub>2</sub> chemisorption, the sample was purged in He flow for 10 min and its temperature was then increased to 700 °C ( $\beta = 30$  °C min<sup>-1</sup>, H<sub>2</sub>-TPD). The H<sub>2</sub> signal ( $m/z = 2$ ) was continuously monitored with online mass spectrometer (MS, Balzers, Omnistar 1-200 amu) and converted into concentration (mol%) using a certified gas mixture (0.95 vol% H<sub>2</sub>/He). Based on the material balance for an open-flow reactor, the rate of H<sub>2</sub>

desorption was estimated; the accumulation term for this dynamic experiment was found to be very small compared to the other terms of the material balance. Based on the nickel dispersion,  $D_{Ni}$  (%), the mean particle size, ( $d_{Ni}$ , nm) was estimated (Eq. (7)) [20] and compared to that obtained by PXRD studies.

$$d_{Ni} (\text{nm}) = 0.97 D_{Ni}^{-1} \quad (7)$$

#### 2.4. Dry reforming of methane (DRM) catalytic performance

The catalytic performance of the supported Ni catalysts for the DRM reaction was examined on a home-made gas-flow system [57]. A 0.1-g of the catalyst calcined at 750 °C/2 h (static air, furnace) were finely ground and sieved to less than 106 µm (to minimize internal mass transport effects) and in situ reduced ( $H_2$ , 1 bar) at 750 °C/2 h (fresh sample). Catalytic measurements for DRM were performed using a 20 vol%  $CH_4$ /20 vol%  $CO_2$ /60 vol% He feed gas stream at 750 °C with a flow rate of 50  $\text{NmL min}^{-1}$  (GHSV of ~30,000  $\text{h}^{-1}$ ). The effluent gas stream was continuously monitored by online Mass Spectrometer (MS) for  $H_2$  ( $m/z = 2$ ),  $CH_4$  ( $m/z = 15$ ),  $CO$  ( $m/z = 28$ ), and  $CO_2$  ( $m/z = 44$ ), and an IR gas analyzer (Horiba, Model VA-3000) for  $CO/CO_2$ , which was connected in series to the MS. Quantification of the respective signals was made by using certified calibration gas mixtures, ca. 1.06 vol%  $CO$ /1.02 vol%  $CH_4$ /0.95 vol%  $H_2$ /He, and 2.55 vol%  $CO_2$ /He. The catalytic activity of the solids in terms of  $CH_4$  and  $CO_2$  conversions ( $X_{CH_4}$  and  $X_{CO_2}$ , %) was evaluated via Eq. (8). The product yields of hydrogen,  $Y_{H_2}$  (%) and  $CO$ ,  $Y_{CO}$  (%) were estimated using Eqs. (9) and (10), respectively:

$$X_i (\%) = \frac{F_i^{in} - F_i^{out}}{F_i^{in}} \times 100 \quad (8)$$

$$Y_{H_2} (\%) = \frac{F_{H_2}^{out}}{2F_{CH_4}^{in}} \times 100 \quad (9)$$

$$Y_{CO} (\%) = \frac{F_{CO}^{out}}{F_{CH_4}^{in} + F_{CO_2}^{in}} \times 100 \quad (10)$$

In Eqs. (8)–(10),  $F_i^{in}$  and  $F_i^{out}$  are the molar flow rates ( $\text{mol s}^{-1}$ ) of reactant  $i$  ( $CH_4$  or  $CO_2$ ) and product ( $H_2$  or  $CO$ ) at the inlet and outlet of the reactor, respectively. The  $F_i^{out}$  was estimated based on the total molar flow rate at the outlet of reactor and the mole fraction of reactant or product measured by MS and IR gas analyzers. External mass transport effects were practically absent after obtaining same (within less than 5%)  $CH_4$  conversion at two different W/F values (0.1 g/50  $\text{NmL min}^{-1}$ ; 0.2 g/100  $\text{NmL min}^{-1}$ ).

#### 2.5. Characterization of carbon

##### 2.5.1. Dry reforming of methane (DRM) reaction

The amount ( $\text{mg C g}_{\text{cat}}^{-1}$  or wt%) and reactivity towards oxygen of deposited carbon after 12 h or 100 h of DRM (20 vol%  $CH_4$ ,  $CH_4/CO_2 = 1$ ) at 750 °C were examined via temperature-programmed oxidation (TPO) experiments. A 20-min He purge and a temperature increase to 800 °C in He gas flow, following DRM, was applied to ensure that no  $CO_2$ ,  $CO$ ,  $H_2$  or  $CH_4$  were left in the gas lines (their respective MS signals reached their background values), and likely formed adsorbed carbonate species were decomposed (up to 800 °C). The transient response curves of  $CO$  and  $CO_2$  recorded by MS were also used to estimate the equivalent amount of carbon removed from the catalyst surface during this He gas thermal treatment. The catalyst temperature was then decreased to 100 °C, and the feed was switched to 10 vol%  $O_2$ /He (50  $\text{NmL min}^{-1}$ ) to initiate a TPO (100–800 °C,  $\beta = 30 \text{ }^{\circ}\text{C min}^{-1}$ ) during which the MS signals of  $CO$  and  $CO_2$  ( $m/z = 28$  and 44, respectively) were continuously monitored; their conversion to mol% was made after using

certified calibration gas mixtures, ca. 1.06 vol%  $CO$ /He and 2.55 vol%  $CO_2$ /He. The appropriate material balance was used to report carbon oxidation rate vs temperature profiles.

##### 2.5.2. $CH_4$ decomposition reaction (20 vol% $CH_4$ /He)

The dynamics of methane decomposition in the absence of  $CO_2$  and that of carbon deposition were of interest in this work. The initial transient rate of  $CH_4$  decomposition on a practically free of carbon Ni surface was estimated during the step-gas concentration switch  $\text{He} \rightarrow 20 \text{ vol\% } CH_4/\text{He}$  (750 °C, t). The catalyst ( $W = 20 \text{ mg}$ ;  $\text{SiC} = 30 \text{ mg}$ ;  $F_T = 50 \text{ NmL min}^{-1}$ ) was kept for 30 min in  $CH_4/\text{He}$ , and the evolution of  $H_2$ ,  $CH_4$  and  $CO$  gases was continuously monitored with MS ( $m/z = 2$ , 15 and 28, respectively). A 10-min He purge was then conducted at 750 °C, followed by an increase of the catalyst temperature to 800 °C, where the catalyst was kept at 800 °C until both  $CO$  and  $CO_2$  MS signals reached their background values. The catalyst temperature was then decreased to 200 °C, and the feed was changed to 10 vol%  $O_2/\text{He}$  (50  $\text{NmL min}^{-1}$ ) followed by a temperature increase to 800 °C for a TPO run ( $\beta = 30 \text{ }^{\circ}\text{C min}^{-1}$ ). During TPO,  $CO$  ( $m/z = 28$ ) and  $CO_2$  ( $m/z = 44$ ) MS signals were continuously monitored, based on which the equivalent amount of carbon accumulated during the 30-min  $CH_4/\text{He}$  gas treatment was estimated.

##### 2.5.3. $CO$ disproportionation reaction (20 vol% $CO/\text{He}$ )

The dynamics of the reverse Boudouard reaction (second route responsible for the formation of inactive carbon in the DRM) was studied by the step-gas concentration switch  $\text{He} \rightarrow 20 \text{ vol\% } CO/\text{He}$  (t) at 750 °C. The initial transient rate of  $CO$  dissociation was estimated, and the amount of carbon accumulated after 30 min in  $CO/\text{He}$  was obtained following TPO (200–800 °C,  $\beta = 30 \text{ }^{\circ}\text{C min}^{-1}$ ; 10 vol%  $O_2/\text{He}$ ) as in the  $CH_4/\text{He}$  reaction. During the transient experiment ( $W = 20 \text{ mg}$ ;  $\text{SiC} = 30 \text{ mg}$ ;  $F_T = 50 \text{ NmL min}^{-1}$ ), the evolution of  $CO$  conversion and  $CO_2$  formation rates were followed by online MS ( $m/z = 28$  and 44, respectively).

#### 2.6. Quantification of the oxidation of carbon by lattice oxygen of support during DRM

To quantify the participation of support's lattice oxygen in the oxidation of carbon derived mainly by the  $CH_4$  activation route and significantly less by the reverse Boudouard reaction [15,17,21], the  $^{16}\text{O}$  of the support was first exchanged for  $^{18}\text{O}$  (more than 80%) after the step gas switch  $\text{Ar} \rightarrow 2 \text{ vol\% } ^{18}\text{O}_2/2 \text{ vol\% Kr/Ar}$  (15 min) at 750 °C was conducted on the fresh catalyst sample (Section 2.2;  $W = 20 \text{ mg}$ ;  $\text{SiC} = 30 \text{ mg}$ ;  $F_T = 50 \text{ NmL min}^{-1}$ ). During the latter gas treatment, the MS signals of  $^{16}\text{O}_2$  ( $m/z = 32$ ),  $^{16}\text{O}^{18}\text{O}$  ( $m/z = 34$ ),  $^{18}\text{O}_2$  ( $m/z = 36$ ) and  $\text{Kr}$  ( $m/z = 84$ ) were recorded continuously with online MS. Conversion of the transient response curves of  $^{16}\text{O}_2(\text{g})$  ( $m/z = 32$ ) and  $^{16}\text{O}^{18}\text{O}(\text{g})$  ( $m/z = 34$ ) MS signals into concentration (mol%), and the estimation of the amount of oxygen exchanged ( $\text{mol } ^{16}\text{O g}^{-1}$ ) was made after calibration of the MS signals and use of appropriate material balances, as reported elsewhere [58].

The temperature of the catalyst was then decreased quickly (ca. < 5 min) to 400 °C in the  $^{18}\text{O}_2/\text{Ar}$  gas mixture, followed by a 10-min Ar purge and a switch to pure  $H_2$  for 1 h. The latter  $H_2$  gas treatment was made to ensure that practically all the  $\text{Ni}^{18}\text{O}$  formed under the  $^{18}\text{O}_2/\text{Ar}$  gas mixture would be in metallic state ( $\text{Ni}^0$ ), active for the DRM reaction. At the same time, only a small amount of support's lattice  $^{18}\text{O}$  was reduced by  $H_2$  at 400 °C. The latter was confirmed by a separate experiment after measuring the amount of consumed  $H_2$  during the switch  $\text{Ar} \rightarrow 5\% H_2/\text{Ar}$  (t) at 400 °C, following the same catalyst pre-treatment described above.

Following  $H_2$  reduction (1 bar, 400 °C), the feed gas stream was switched to Ar gas for a 10-min purge (until no MS signals for  $H_2$  were observed), and the temperature was then increased in Ar flow to 750 °C. The feed was then switched to the DRM gas mixture (20%  $CH_4/20\%$

$\text{CO}_2/2\%\text{Ar}/\text{He}$ ,  $F_T = 50 \text{ NmL min}^{-1}$ ), during which the isotopic  $\text{C}^{16}\text{O}$  and  $\text{C}^{18}\text{O}$  transient response curves were followed by online MS. These responses describe the dynamics of carbon oxidation by  $^{16}\text{O}$  ( $\text{CO}_2$  activation route) and by  $^{18}\text{O}$ -lattice oxygen of support, respectively, under DRM reaction conditions [21]. At the switch to the DRM gas mixture, however, the formation of  $\text{C}^{16}\text{O}^{18}\text{O}$  and  $\text{C}^{18}\text{O}_2$  due to exchange reactions between  $\text{C}^{16}\text{O}_2$  and  $^{18}\text{O}_L$ , followed by reforming with  $\text{CH}_4$  might take place, thus producing  $\text{C}^{18}\text{O}(\text{g})$  [21]. To check this possibility for the correct interpretation of the dynamic evolution of  $\text{C}^{18}\text{O}(\text{g})$  formation rate, the last switch to the DRM gas mixture was replaced by the step-gas switch to a 20 or 10 vol%  $\text{CO}_2/\text{Ar}$ , and the transient responses of  $\text{C}^{16}\text{O}^{18}\text{O}$ ,  $\text{C}^{18}\text{O}_2$  and  $\text{C}^{18}\text{O}$  formation were followed by online MS. Under the 20 vol%  $\text{CO}_2/\text{Ar}$  gas treatment, maximum exchange of  $\text{CO}_2$  with  $^{18}\text{O}_L$  is expected, since it will be shown that under the 2-min duration of the transient experiment, the 20 vol%  $\text{CO}_2$  in the DRM gas mixture was converted to  $\sim 60\%$ . Calibration of the  $\text{C}^{18}\text{O}$  ( $m/z = 30$ ) and  $\text{C}^{16}\text{O}$  ( $m/z = 28$ ) signals to concentration (mol%) was reported [21]. Based on material balance and the measured gas concentrations of  $\text{C}^{16}\text{O}$  and  $\text{C}^{18}\text{O}$ , the respective transient rates per unit mass of catalyst ( $\mu\text{mol g}^{-1}\text{cat s}^{-1}$ ) were estimated; it was found that the accumulation term in the material balance equation was negligible.

### 3. Results and discussion

#### 3.1. Catalysts structure and composition

The elemental composition of the calcined catalysts was evaluated based on SEM-EDX and results are presented in Table S1. It is clearly seen that the EDX values are close to the nominal ones (intended values during the synthesis). Evidence for the introduction of  $\text{Sm}^{3+}$  ( $1.02 \text{ \AA}$ ) and  $\text{La}^{3+}$  ( $1.1 \text{ \AA}$ ) in the lattice structure of Ce-10Cu-O support is depicted in Fig. 1A (powder XRD patterns) after calcination of the supported Ni

catalysts at  $750^\circ\text{C}$ ; for comparison the Ni/Ce-10Cu-O diffractogram is also shown (Fig. 1A, c). The diffraction peaks recorded at  $\sim 28.5$ ,  $33.1$ ,  $47.5$  and  $56^\circ 2\theta$  correspond to reflections due to the (111), (200), (220) and (311) planes, respectively, of the cubic fluorite structure of  $\text{CeO}_2$  (JCPDS 34-0394) [40,59]. There was a small shift towards smaller diffraction angles after the incorporation of larger cations ( $\text{Sm}^{3+}$  and  $\text{La}^{3+}$ ) and smaller cations ( $\text{Cu}^{2+}$ ) than  $\text{Ce}^{4+}$  (45Ce-45Sm-10Cu-O and 45Ce-45La-10Cu-O) compared to the XRD patterns of Ce-La-O [40] and Ce-Sm-O [38,60]. Additionally, the absence of characteristic diffraction peaks of pure phase could first suggest the formation of a homogeneous solid solution phase with  $\text{La}_2\text{O}_3$  and  $\text{Sm}_2\text{O}_3$  as minor phases that escape XRD detection (very low wt% composition in the multiphase system) [61]. This means that  $\text{Ce}^{4+}$  cations in the ceria lattice were partly substituted for  $\text{Sm}^{3+}$  and  $\text{La}^{3+}$  heteroatoms, thus leading to the formation of oxygen vacant sites ( $\text{O}_v$ ) due to the alio-valent heteroatom substitution in the ceria lattice [62]. Raman studies to follow provided evidence for the presence of  $\text{MO}_8$  moieties in the ceria lattice. Additionally, copper oxide and cerium-copper oxide hetero-phases were not observed in the present powder X-ray diffractograms (Fig. 1A), which coincides with our earlier findings over Ce-La- $x$ Cu-O ( $x = 0-20$  at%) mixed metal oxides [40]. It seems that a medium content of Cu (10 at%) can be accommodated in the ceria lattice. On the other hand, HRTEM and STEM-EDX microstructural studies to be presented and discussed in the following Section 3.2, revealed the presence of NiCu alloy nanoparticles in both catalytic systems not detected by powder X-ray diffraction.

The most intense peak associated with the (111) plane was used to calculate a mean primary crystallite size ( $d_c, \text{nm}$ ) for the support and Ni (see Eq. (6)), and results are presented in Table 1 ( $d_c = 16, 26$ , and  $29.5 \text{ nm}$  for Ce-Sm-10Cu-O, Ce-La-10Cu-O and Ce-10Cu-O, respectively). The mean Ni particle size reported in Table 1 was also estimated via  $\text{H}_2$ -TPD studies (Section 3.3) and a good agreement is noticed.

The  $\text{N}_2$  adsorption-desorption isotherms (BET) of both calcined at  $500$  and  $750^\circ\text{C}$  supported Ni catalysts are shown in Fig. 1B and Fig. S1. It is noted that both isotherms are of type-IV with type-H3 hysteresis, indicating  $\text{N}_2$  condensation in the material's meso-pores during adsorption [63]. The specific surface areas (SSA,  $\text{m}^2 \text{ g}^{-1}$ ) estimated are given in Table 1. Both 5Ni/Ce-La-10Cu-O and 5Ni/Ce-Sm-10Cu-O catalytic systems exhibit low and very similar surface area, ca.  $4.6 \text{ m}^2 \text{ g}^{-1}$  (after calcination at  $750^\circ\text{C}$ ). Based on the SEM images of catalysts (Fig. S2), the crystallites aggregate due to the thermal history/treatment of the samples, to form a foamy-type 3D structure, indicative for the presence of macro-porosity (e.g., pore sizes larger than  $50 \text{ nm}$ ), in agreement with the steep increase of  $\text{N}_2$  uptake at high relative  $\text{N}_2$  gas pressures. In the case of Ce-10Cu-O solid support, the largest SSA was measured ( $11 \text{ m}^2 \text{ g}^{-1}$ ) corresponding also to the largest  $d_c$  ( $29.5 \text{ nm}$ , Table 1).

Raman spectroscopic results of the calcined supported Ni catalysts are expected to provide greater insight on the rather complex oxide sub-lattice structure of supports, complimenting the powder XRD. Oxygen defects formed in the ceria lattice upon doping can be probed, as well as the formation of possible new metal-oxygen bond environments (e.g.,  $\text{LaO}_8$ ,  $\text{SmO}_8$  and  $\text{CuO}$ ) in the case of hetero-phase impurity presence. Fig. 2A shows Raman spectra recorded on the La- and Sm-doped Ce-10Cu-O supported Ni catalysts. Two main peaks at  $\sim 460$  and  $590 \text{ cm}^{-1}$  were recorded indicative of a cubic fluorite structure [64]; the peak centred at  $\sim 461 \text{ cm}^{-1}$  corresponds to the  $\text{F}_{2g}$  vibrational mode of the fluorite oxygen sub-lattice, in agreement with the powder XRD. Also, the  $\text{F}_{2g}$  peak shifted (blue shift) to lower wavelengths compared to pure  $\text{CeO}_2$  (prepared under the same experimental conditions) due to the La/Sm doping [40,41]. After co-doping of La or Sm with Cu, an asymmetric broadening and intensity attenuation of  $\text{F}_{2g}$  peak was observed (lattice disordering).

The second peak appeared at  $590 \text{ cm}^{-1}$  refers to the oxygen vacancies/defects in the lattice due to charge compensation, which cannot be seen in pure ceria [62]. The deconvolution of the peak at  $590 \text{ cm}^{-1}$

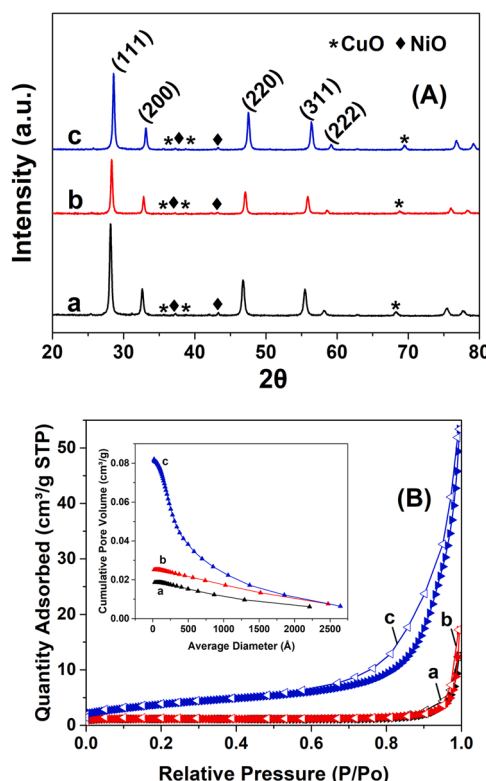
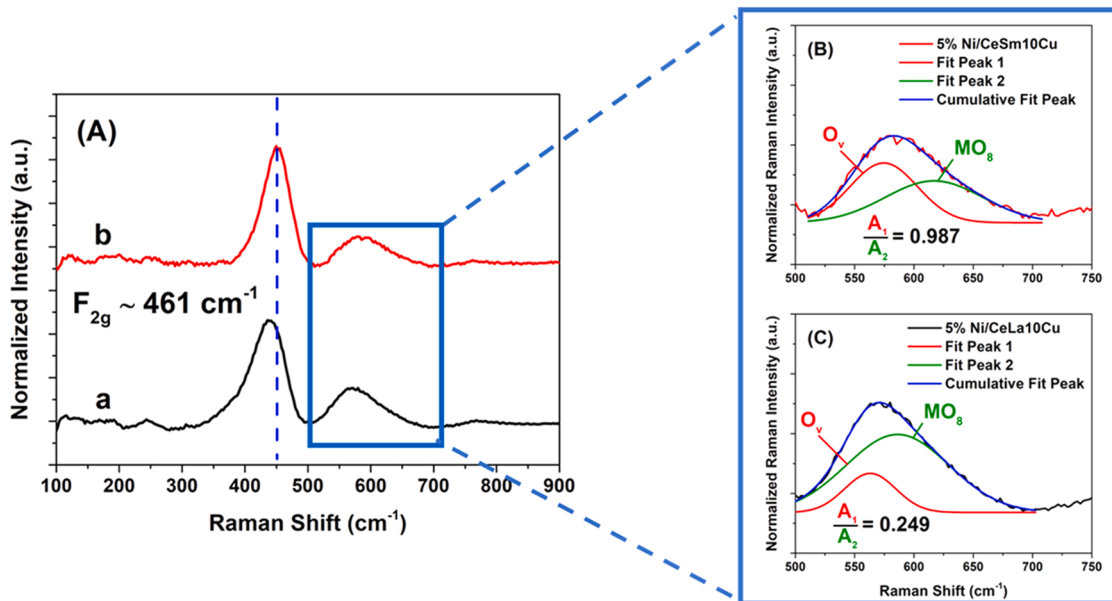


Fig. 1. (A) Powder XRD patterns and (B)  $\text{N}_2$  adsorption-desorption isotherms obtained at  $77 \text{ K}$  along with the cumulative pore volume ( $\text{cm}^3/\text{g}$ ) (inset) for the 5 wt% Ni supported on (a) Ce-La-10Cu-O, (b) Ce-Sm-10Cu-O and (c) Ce-10Cu-O carriers following calcination at  $750^\circ\text{C}/2 \text{ h}$ .

**Table 1**

Structural and textural characteristics of 5 wt% Ni supported on Ce-La-10Cu-O, Ce-Sm-10Cu-O and Ce-10Cu-O carriers.

Sample 5 wt% Ni/support	Mean primary crystallite size, $d_c$ (nm) of doped ceria phase	Mean crystallite size of NiO, $d_{NiO}$ (nm)	Mean Ni crystallite size, $d_{Ni}$ (nm)	SSA ( $m^2/g$ )
Ce-La-10Cu-O	26 <sup>a</sup>	31.0	26.3 <sup>a</sup> 23.5 <sup>bc</sup>	3.40 <sup>c</sup> $4.6^d \pm 0.3$
Ce-Sm-10Cu-O	16 <sup>a</sup>	23.1	19.6 <sup>a</sup> 17.0 <sup>b</sup>	$24.6^c \pm 0.6$ $4.7^d \pm 0.5$
Ce-10Cu-O	29.5	28.3	24.1 <sup>a</sup>	$11.3^d \pm 0.4$

<sup>a</sup> Estimated from powder XRD (use of Scherrer relationship,  $K = 0.9$ ) and after using Eq. (6).<sup>b</sup> Based on  $H_2$  chemisorption followed by TPD.<sup>c</sup> Following calcination at 500 °C.<sup>d</sup> Following calcination at 750 °C.**Fig. 2.** (A) Raman spectra of 5 wt% Ni/Ce-La-10Cu-O (black curve, a) and 5 wt% Ni/Ce-Sm-10Cu-O (red curve, b) catalysts. Deconvolution of Raman spectra in the 500–700  $cm^{-1}$  region for the 5 wt% Ni/Ce-Sm-10Cu-O (B) and 5 wt% Ni/Ce-La-10Cu-O (C) catalysts.

for both catalysts was conducted to uncouple the formation of  $O_v$  (coordinatively unsaturated site) and  $MO_8$ -hetero-phase impurities contribution [30]. These defect bands can be clearly seen in the deconvoluted Raman spectra shown in Fig. 2B (Ni/Ce-Sm-10Cu-O) and C (Ni/Ce-La-10Cu-O). The  $I_{Ov}/I_{F2g}$  intensity ratio was used as a descriptor parameter of the oxygen vacancy population in the support. The Sm- and La-doped supported Ni catalysts showed a  $I_{Ov}/I_{F2g}$  ratio value of 0.18 and 0.13, respectively. The larger the  $I_{Ov}/I_{F2g}$  ratio value the higher the oxygen vacant sites concentration in the structure, to be discussed later (Section 3.9). In addition, it can be observed that the intensity loss of  $O_v$  band for the 5 wt% Ni/Ce-La-10Cu-O catalyst is accompanied by an increase of the  $MO_8$  vibrational band intensity corresponding to the hetero-phase impurity [30]. This is also reflected in the change of the  $(A_1/A_2)$  ratio, where  $A_1$  and  $A_2$  are the areas corresponding to the Raman bands of the  $O_v$  and  $MO_8$  entities, respectively. Previous work using transient  $^{16}O/^{18}O$  isotopic exchange experiments performed over the Ce-La-xCu-O supports showed that oxygen diffusion rates are correlated to the type of heteroatom, content and oxygen vacancy order/disorder, which induce local strains [40].

The  $O_v$  can be found in two types of arrangements, ordered or disordered clusters. Mori et al. [65] and Ou et al. [66] examined the microstructure of ceria lattice with  $Sm^{3+}$  and  $La^{3+}$  heteroatoms, and they found that the oxygen vacant sites can exist in both the above-mentioned arrangements in a crystal nano-domain. Generally, ordered oxygen vacant sites occur in the case of co-doping of ceria.

Previous work [24] on similar Ce-La-xCu-O ( $x = 3$ –20 at%) solids argued that the higher oxygen mobility in the Cu- and La-doped ceria lattice is due to the lower lattice strain mechanism compared to pure  $CeO_2$ , whereas the hindering of oxygen vacancies is attributed to the configurational entropy ordering.

### 3.2. HR-TEM microstructural studies – fresh catalysts

Fig. 3A shows a HRTEM image recorded over the fresh Ni/Ce-La-10Cu-O catalyst following re-calcination at 750 °C/2 h and reduction at 750 °C/2 h. The lattice fringes observed give an interplanar d-spacing of  $\sim 0.32$  nm, which is very close to the d-spacing of (111) planes in  $CeO_2$  crystals (0.32 nm) [67]. Red-Green-Blue (RGB) mappings of Ni/Ce-La-10Cu-O and Ce-La-10Cu-O supports alone are also depicted in Fig. 3B and C, respectively, at comparable magnifications. From the RGB analysis of the supported Ni catalyst, it can be stated that Cu species tend to diffuse towards the surface and agglomerate with Ni (Fig. 3B), in a rather homogeneous fashion, giving rise to the formation of  $NiCu$  alloy crystallites of 25–30 nm in size. This might be facilitated by the reducing gas environment ( $H_2$  at 750 °C) applied prior to imaging, responsible for the creation of additional oxygen vacancies in the ceria matrix. The high temperature used during the pre-treatment step of Ni/Ce-La-10Cu-O increased the Ni-Cu interdiffusion rates [68], leading eventually to NiCu alloying (Fig. 3B). STEM-EDX analysis at different locations (Fig. S3, B-E) demonstrated the co-presence of Ni and Cu in the particles.

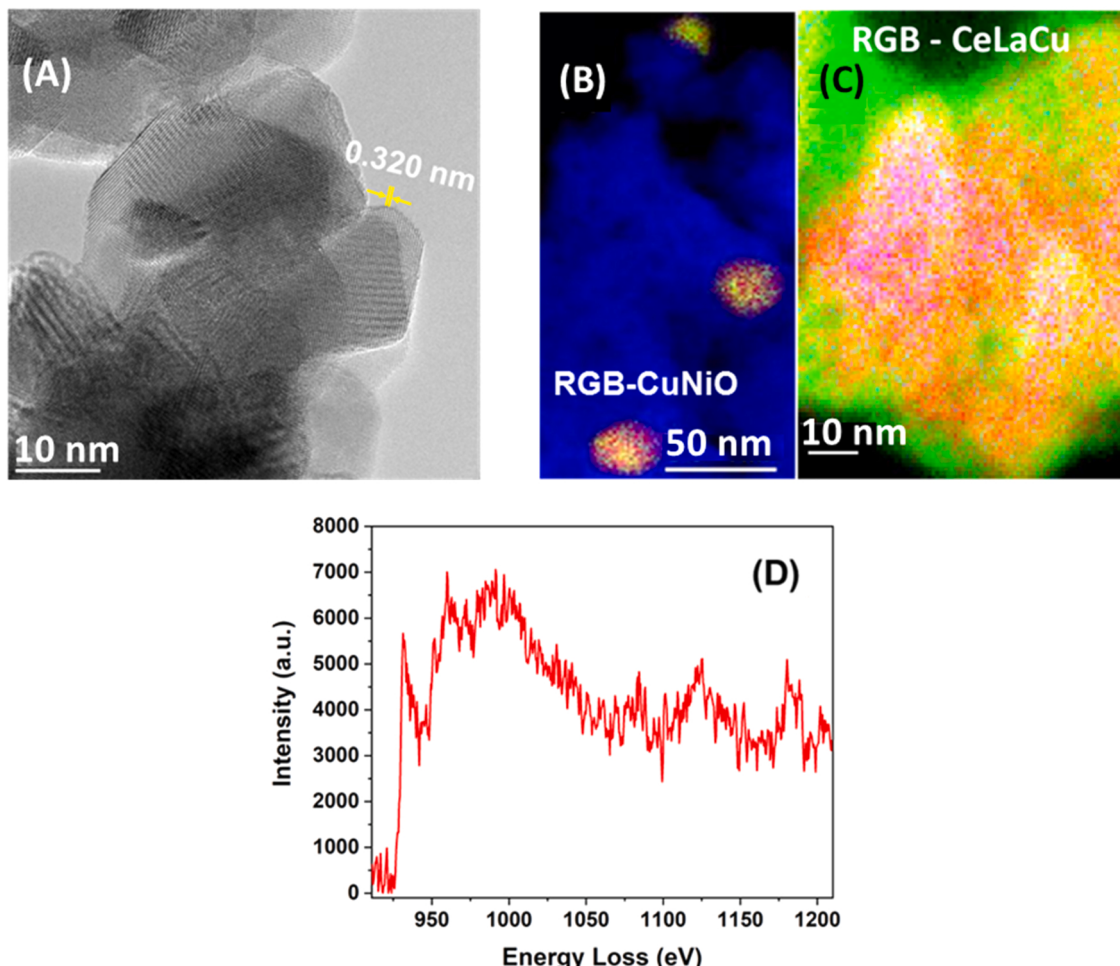


**Fig. 3.** (A) HRTEM image and (B) Red-Green-Blue (RGB) mapping analysis of the fresh 5 wt% Ni/Ce-La-10Cu-O catalyst. Red (R): Cu, Green (G): Ni, Blue (B): O. (C) RGB analysis of the Ce-La-10Cu-O support alone. Red (R): Ce, Green (G): La, Blue (B): Cu. (D) Cu EELS.

The composition of the alloy was estimated based on EELS analysis, and it was found to be  $\text{Ni}_{0.66}\text{Cu}_{0.34}$ . Additionally, using the EELS spectra from several NPs, such as the one shown (dashed box area) in Fig. S4A, the concentration of 6.4 at% for O was determined after applying the multi-linear least square (MLLS) fitting method (Fig. S4B). In the RGB analysis shown in Fig. 3B, the Blue (B) signal originates from support oxygen.

In the case of Ce-La-10Cu-O support alone (Fig. 3C), following calcination at 750 °C only, Cu is rather homogeneously embedded in the La-doped ceria lattice, in agreement with previous findings reported by AlKetbi et al. [40]. The high temperature reduction in  $\text{H}_2$  gas atmosphere for the formation of NiCu alloy is consistent with other reports, where XPS and Auger spectroscopic studies on NiCu alloys showed that at  $T > 700$  °C, surface enrichment by Cu did occur [69]. Similarly, in-situ reduction experiments performed at 300 °C under 20%  $\text{H}_2/\text{N}_2$  gas atmosphere on NiCu bimetallic catalysts showed that Ni and Cu were uniformly alloyed, and only 13% segregated to form a Ni-rich surface [68]. Cu EELS spectrum confirmed the metallic state of Cu (Fig. 3D).

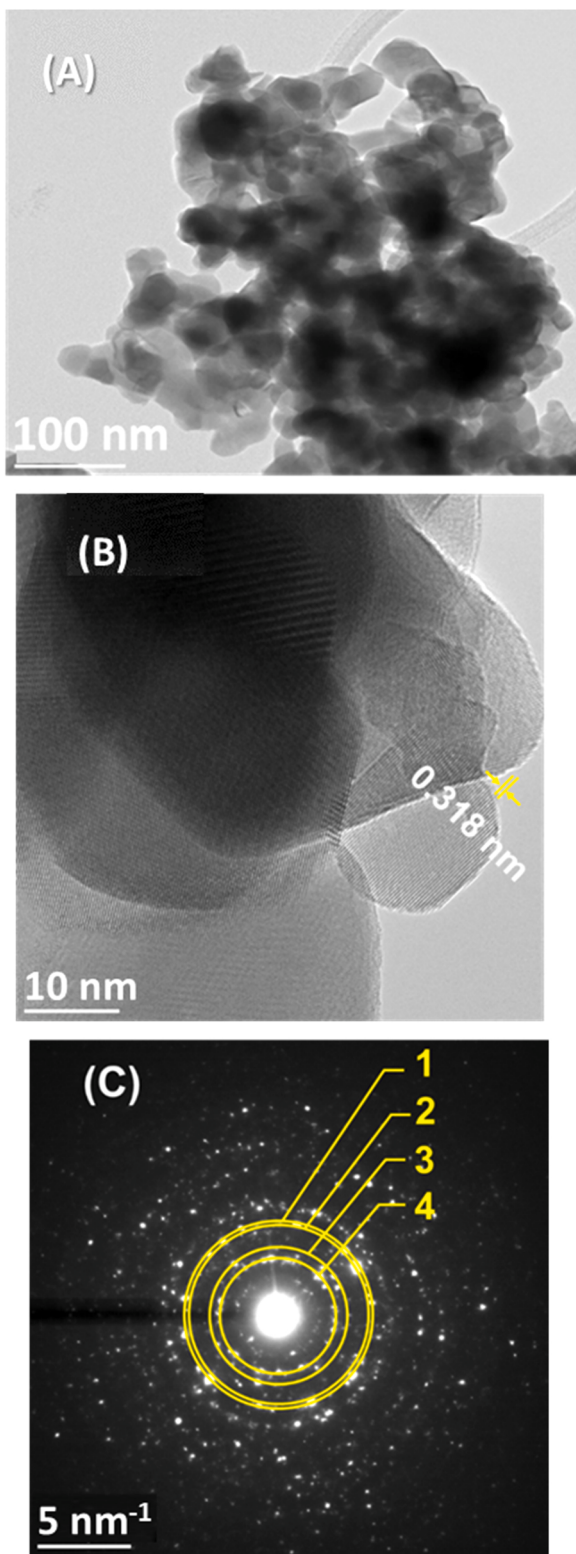
Fig. S5a depicts the SAED pattern of the fresh 5 wt% Ni/Ce-La-10Cu-O catalyst, showing a polycrystalline pattern with inter-planar d-spacings of 0.157 and 0.397 nm, likely corresponding to single crystal  $\text{CeO}_2$  (100) [70]. The EDX spectrum of 5 wt% Ni/Ce-La-10Cu-O fresh catalyst depicted in Fig. S5b confirms the presence of Ni, Cu, La, and Ce elements.

Fig. 4A and B shows HRTEM images obtained over the fresh Ni/Ce-Sm-10Cu-O catalyst following re-calcination at 750 °C/2 h and reduction at 750 °C/2 h. A magnified region of image (A) is shown in Fig. 4B,

where the lattice fringes with inter-planar d-spacing of 0.318 nm are observed, associated with the (002) facet in  $\text{CeO}_2$  [71]. This can be also seen in the SAED pattern, where all the fringes are marked (Fig. 4C), based on which the Ce-Sm-10Cu-O support appears as polycrystalline with inter-planar d-spacings of  $\sim 0.196$  (ring 1), 0.206 (ring 2), 0.27 (ring 3), and 0.32 nm (ring 4, Fig. 4C), corresponding to fringes of Cu in tetragonal coordination [72], metallic Ni (111), fringes of (200) facet in  $\text{CeO}_2$  [71], and fringes of the (111) facet in  $\text{CeO}_2$  [73], respectively. The d-spacing values for the Ni/Ce-La-10Cu-O and Ni/Ce-Sm-10Cu-O catalysts are provided in Tables S2–S4. Due to the proximity of the d-spacing values in some cases (e.g., metallic Cu at 0.196 and  $\text{CeO}_2$  (220) at 0.193 nm), Cu EELS was analyzed (Fig. 3D), and this proved the presence of metallic Cu in the solid.

Fig. S6A presents a HAADF-STEM micrograph of the fresh Ni/Ce-Sm-10Cu-O solid, whereas Fig. S6, B–D shows EELS elemental maps of O (B), Ce (C) and Sm (D), which infer their atomic homogeneously dispersion in the support matrix, something that can be associated with the microwave synthesis method applied. On the other hand, in the case of Cu and Ni, it can be noticed that these transition metals tend to agglomerate with each other on the surface, as evidenced by the EELS maps and RGB (ONiCu) elemental distribution shown in Fig. S6E–F and G, respectively. It is noted that the cyan color in the RGB mapping (Fig. S6G) is the result of NiCu alloy formation (green and blue).

Fig. S6H depicts the EEL spectrum indicating the white edges of Ni, Cu, Ce and Sm of the same region in the Ni/Ce-Sm-10Cu-O catalyst. It is noteworthy to state that the white edges of Ni and Cu are not prominently shown in the EEL spectrum of Ni/Ce-La-10Cu-O, since Ce and La



**Fig. 4.** (A) Low magnification and (B) High magnification HRTEM images of fresh 5 wt% Ni/Ce-Sm-10Cu-O catalyst, where lattice fringes with d-spacing of 0.318 nm are observed. (C) Selected Area Electron Diffraction (SAED) pattern with marked (1–4) lattice fringes.

white edges are close to the white edges of Ni and Cu (interference). Additionally, a lower amount of Ni and Cu in the region analyzed on the surface of Ni/Ce-La-10Cu-O can also explain the low intensity of Ni and Cu white edges.

### 3.2.1. Overview on the structure

Based on the powder XRD, Raman, HRTEM/STEM and RGB mapping data, the following conclusions can be withdrawn. Given the similar ionic radii of  $\text{Ce}^{4+}$ ,  $\text{La}^{3+}$  and  $\text{Sm}^{3+}$ , in principle it would be expected to have a solid solution in a wide range of compositions [74]. For the Sm case, it has been reported that  $\text{CeO}_2$ - $\text{Sm}_2\text{O}_3$  can form solid solutions at  $\text{Sm}_2\text{O}_3$  content < 50 at% [75]. In the present Ce-40La(or Sm)-10Cu-O support composition, stable  $\text{La}_2\text{O}_3$  and  $\text{Sm}_2\text{O}_3$  phases have been formed but as *impurity phases*, as proved by Raman. In addition, RGB analysis (Fig. 3C) proves the neighboring co-existence of Ce and La elements. Though, the red and the green colors are not mixed into a new color (each one can be clearly seen as independent color) due to the high percentage of La (45%), thus probing the likelihood of impurity phase formation, as proved by Raman. Based on our previous studies [76], it was found that Cu content up to 10 at% forms a homogeneous solid solution with  $\text{CeO}_2$ -phase; no  $\text{CuO}$  separate phase was identified. In the present work, a very weak  $\text{CuO}$  peak was identified in the powder XRD, where part of the Cu diffused towards the surface and formed alloy with Ni ( $\text{Ni}_{0.66}\text{Cu}_{0.34}$  composition) as shown in Fig. 3B and Fig. S3.

### 3.3. Supported Ni surface characterization by $\text{H}_2$ chemisorption/TPD

Fig. 5 shows  $\text{H}_2$ -TPD traces (in terms of  $\text{H}_2$  desorption rate) of the supported Ni particles on La-doped (Fig. 5a) and Sm-doped ceria (Fig. 5b) carriers. Both desorption spectra have similar features, namely, a main peak at  $\sim 260$  °C accompanied by a shoulder at the high-T side of the peak, ending at  $\sim 450$  °C, and a clear shoulder at the low-T side of the peak. The latter appears at lower temperature ( $\sim 185$  °C) for Ni supported on La-doped ceria carrier. Based on the amount of desorbed hydrogen, and assuming  $\text{H}/\text{Ni}_s$  of 1:1, a Ni dispersion of 4.2% and 5.9%, respectively, was measured for the 5 wt% Ni/Ce-La-10Cu-O and 5 wt% Ni/Ce-Sm-10Cu-O catalytic systems. A mean Ni particle size ( $d_{\text{Ni}}$ , nm) of  $\sim 23.5$  and 17 nm, respectively, was estimated, in good agreement with the powder XRD measurements (Table 1, Fig. S7). The fact that for the two Ni particle sizes of  $\sim 18$  and 25 nm (Table 1, avg. values) the types of surface Ni sites and their distribution is expected to be similar [21, 77], the obtained  $\text{H}_2$ -TPD features (Fig. 5a and b, shape and position) suggest that the support chemical composition influenced slightly only the electronic structure of Ni surface sites and more likely those at the Ni-support interface; the shoulder appeared at the low-T side of the desorption peak (Fig. 5a and b) might be related to this. After comparing the  $\text{H}_2$ -TPD traces, it appears that NiCu alloy nanoparticles identified by HR-TEM in both catalysts (see Section 3.2) are either of low number density compared to Ni, or they possess similar  $\text{H}_2$  desorption characteristics.

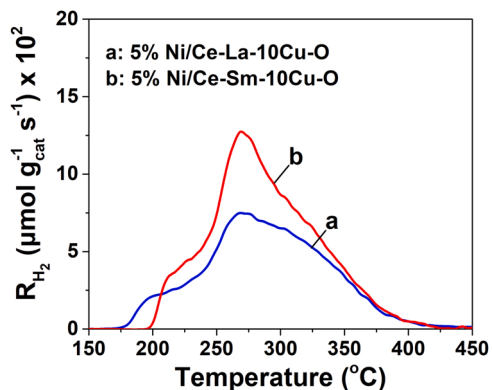


**Fig. 5.**  $\text{H}_2$ -TPD traces in terms of hydrogen desorption rate ( $\mu\text{mol g}^{-1} \text{cat}^{-1} \text{s}^{-1}$ ) obtained on (a) 5 wt% Ni/Ce-La-10Cu-O and (b) 5 wt% Ni/Ce-Sm-10Cu-O catalysts.  $F_{\text{He}} = 50 \text{ NmL min}^{-1}$ ;  $\beta = 30 \text{ }^{\circ}\text{C min}^{-1}$ ;  $W_{\text{cat}} = 0.1 \text{ g}$ .

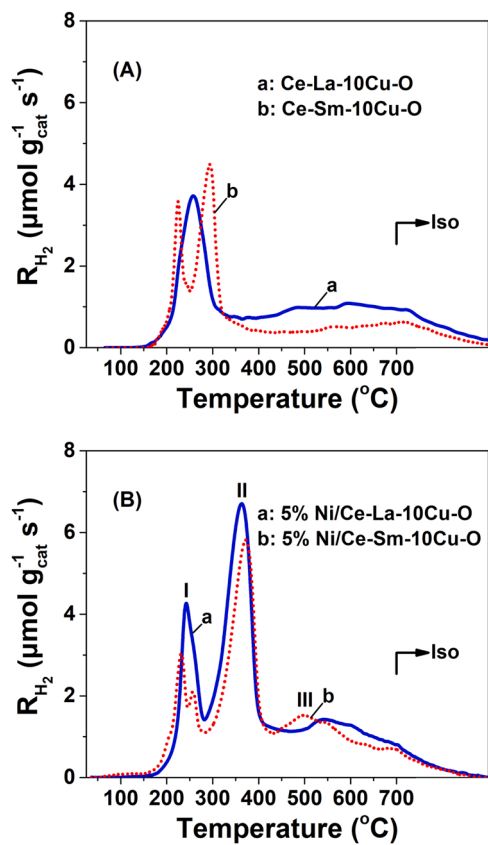


**Fig. 6.** (A) H<sub>2</sub>-TPR traces obtained over the Ce-La-10Cu-O (a) and Ce-Sm-10Cu-O (b) supports, and (B) over the 5 wt% Ni/Ce-La-10Cu-O (a) and 5 wt% Ni/Ce-Sm-10Cu-O (b) catalysts.  $F_T = 50 \text{ NmL min}^{-1}$ , 5.18 vol% H<sub>2</sub>/He;  $\beta = 30 \text{ }^{\circ}\text{C min}^{-1}$ ;  $W_{\text{cat}} = 0.1 \text{ g}$ .

#### 3.4. Catalysts reducibility - H<sub>2</sub> TPR studies

Supported Ni catalysts on reducible MO<sub>x</sub> supports present H<sub>2</sub> reduction peaks at low temperatures (T < 300 °C), in the 300–450 °C range, and at higher temperatures (T > 450 °C), and these are due in general to: (i) NiO and support MO<sub>x</sub> surface species, (ii) support MO<sub>x</sub> species in the sub-surface region, and (iii) MO<sub>x</sub> species in the bulk of the solid, respectively [78–81]. Fig. 6A and B shows H<sub>2</sub>-TPR traces of the Ce-La-10Cu-O and Ce-Sm-10Cu-O supports alone and of the corresponding supported Ni catalysts, respectively. Pure CuO particles main reduction peak appears at 295 °C [78], while that of pure NiO at 350–400 °C [79]. In the case of Ce-La-Cu-O support (Fig. 6A), the major reduction peak at 255 °C corresponds to the reduction of CuO. This result indicates the facilitation of CuO reduction in the presence of Ce-La-O phase, and the strong interaction between the two phases. Also, reduction of Ce-Cu-O phase can take place at this region. In the region of T > 400 °C, the sub-surface and bulk of ceria was reduced (e.g., Ce<sup>4+</sup> → Ce<sup>3+</sup>).

In the case of Ni/Ce-La-10Cu-O catalyst (Fig. 6B), a peak at ~ 240 °C (peak I) is observed, which is ascribed to reduction of Cu<sup>2+</sup> in the presence of Ce-La-Cu-O phase. According to Yang et al. [80], reduction peaks at 213 and 247 °C in the H<sub>2</sub>-TPR profile of Cu<sub>0.10</sub>Ce<sub>0.90</sub>O<sub>2</sub> indicate reduction of finely dispersed copper species on the surface of ceria, in good agreement with the present results. The second reduction peak at 350 °C (peak II) can be linked to the reduction of NiO adjacent to the Ce-La-O phase. The reduction peak at ~ 550 °C followed by a shoulder at the high-T side (Fig. 6B, peak III) is associated with sub-surface and bulk oxygen in ceria [80]. Additionally, high temperature reduction peaks can be attributed to reduction of copper ions that act as substitutional defects in the ceria lattice [80].

In the case of Ce-Sm-10Cu-O support (Fig. 6A), the peaks (almost appeared as doublet) at 210 and 300 °C correspond to the reduction of different sizes of CuO nanoparticles, which are in different interaction with the ceria-related phase (Ce-Sm-O). The second reduction peak (300 °C) can have contributions from the CuO particles interacting with the surface of ceria and/or reduction of ceria surface. In the case of Ni/Ce-Sm-10Cu-O catalyst (Fig. 6B), the reduction peak (doublet) at ~ 220 and 250 °C corresponds to CuO reduction. The doublet peak shape in the case of supported Ni catalyst appears different compared to the doublet peak observed in the Ce-Sm-Cu-O support alone. This is evidence of the alteration of the individual electronic/coordination features of Cu in the presence of Ni (Ni-Cu alloy formation). In addition, it has been reported by Ardiyanti et al. [81] that the enhanced reducibility of NiO species can be linked to the formation of NiO–CuO solid solution, which results from the proximity of NiO and CuO species. A large main reduction peak at ~ 360 °C, followed by a broad reduction peak centred at ~ 500 °C (Fig. 6B) correspond to NiO reduction.

The amount of H<sub>2</sub>(g) consumed, which is equivalent to the quantity of oxygen removed from the solids, was found to be 2.14 and 1.85 mmol O g<sup>-1</sup> for the 5 wt% Ni/Ce-La-10Cu-O and 5 wt% Ni/Ce-Sm-10Cu-O catalysts, respectively. Considering that all 5 wt% Ni was oxidized to NiO (750 °C/2 h) and fully reduced during TPR, then the equivalent amount of oxygen removed was 0.85 mmol O g<sup>-1</sup>, thus resulting in 1.29 and 1.0 mmol O g<sup>-1</sup> reduced from the Ce-La-10Cu-O and Ce-Sm-10Cu-O supports, respectively. In the case of Ce-La-10Cu-O and Ce-Sm-10Cu-O supports alone, the amount of oxygen removed was 1.5 and 1.1 mmol g<sup>-1</sup>, respectively. Given the similar BET areas of the two support materials and the similar number density of surface oxygen ions per exposed facet, the larger reduction ability by hydrogen of Ce-La-10Cu-O can be testified. This result finds good agreement with the H<sub>2</sub>-TPR findings of She et al. [82] for the CuO/CeO<sub>2</sub>-La<sub>2</sub>O<sub>3</sub> solid.

#### 3.5. Characterization of surface basic sites

In principle, CO<sub>2</sub> temperature-programmed desorption (TPD) peaks emerging at temperatures lower than 200 °C, between 200 and 450 °C, and at temperatures higher than 450 °C, represent weak (W), moderate (M), and strong (S) basic sites, respectively [83]. This is correlated with the magnitude of CO<sub>2</sub> adsorption energy as investigated extensively by Hahn et al. [84] via DFT calculations. According to these studies, there are three possible stable CO<sub>2</sub> configurations of adsorbed CO<sub>2</sub> on CeO<sub>2</sub> (111), namely: (i) monodentate carbonate, (ii) bidentate carbonate, and (iii) linearly adsorbed CO<sub>2</sub> species. Linearly adsorbed CO<sub>2</sub> species are weakly adsorbed on the surface O atoms [84,85]. It was reported [18,19,23] that basic supports lead to the reduction of coke accumulation rate during DRM since coke gasification is largely facilitated, to be discussed in a later section.

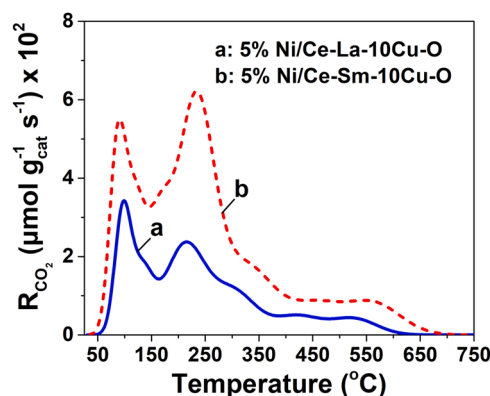


**Fig. 7.** CO<sub>2</sub>-TPD traces obtained over the 5 wt% Ni/Ce-La-10Cu-O (a) and 5 wt% Ni/Ce-Sm-10Cu-O (b) catalysts.  $F_{\text{He}} = 30 \text{ NmL min}^{-1}$ ,  $\beta = 30 \text{ }^{\circ}\text{C min}^{-1}$ ,  $W_{\text{cat}} = 0.1 \text{ g}$ .

The  $\text{CO}_2$ -TPD profiles recorded on the present Ce-La-10Cu-O and Ce-Sm-10Cu-O supported Ni catalysts are shown in Fig. 7. In the case of Ni/Ce-La-10Cu-O (Fig. 7A), two discernible  $\text{CO}_2$  desorption peaks centred at  $\sim 100$  °C (weak basic sites) and  $210$  °C (moderate basic sites) with shoulders on their high-T side were detected. A broad but smaller desorption peak in the  $375$ – $600$  °C range was also observed (strong basic sites). A very similar  $\text{CO}_2$ -TPD trace was found for the Ni/Ce-Sm-10Cu-O solid (Fig. 7B) but of a larger quantity ( $27.9$  vs  $13.3$   $\mu\text{mol CO}_2 \text{ g}^{-1}$ ). Given the fact that the BET surface area is similar for the two supported Ni catalysts (Table 1), the number density of basic sites becomes also larger,  $\sim 2.1$  times in the case of Sm<sup>3+</sup>-doped than La<sup>3+</sup>-doped ceria ( $6.06$  vs.  $2.9$   $\mu\text{mol m}^{-2}$ ). As will be shown later in Section 3.6, the Ni/Ce-Sm-10Cu-O catalyst exhibits significantly larger amounts of accumulated carbon after DRM at  $750$  °C compared to Ni/Ce-La-10Cu-O, suggesting that the number density of basic sites alone is not the crucial factor for reducing coke formation. It was reported [2,86] that the type of surface facet, basic strength, and the different morphologies of metal oxide nanoparticles become important for coke deposition control in the DRM. It will be shown that lattice oxygen mobility is a more important intrinsic property of support in controlling coke formation for the present catalytic systems (see Section 3.9), in agreement also with the  $\text{H}_2$ -TPR results presented and discussed previously. This finds also support from the  $\text{CO}_2$ -TPD results (Fig. 7), where the Sm<sup>3+</sup>-containing support presents a larger fraction of *moderate basic sites*. The surface basic strength relates to the oxygen charge and thus to the binding strength between oxygen anions and metal cations in the lattice, thus to the oxygen mobility. It appears that La<sup>3+</sup>-doped ceria exhibits a larger concentration ( $\mu\text{mol m}^{-2}$ ) of labile surface/subsurface oxygen species with higher mobility than Sm<sup>3+</sup>-doped ceria (Section 3.9).

### 3.6. Dry reforming of methane (DRM) catalytic performance

Table 2 and Fig. 8A present the  $\text{CH}_4$  and  $\text{CO}_2$  conversions (%), the rate of  $\text{CH}_4$  conversion per unit mass of Ni ( $\text{mmol g}^{-1} \text{Ni s}^{-1}$ ), and the amount of carbon ( $\text{mg C g}_{\text{cat}}^{-1}$ ) accumulated after 12 h of DRM at  $750$  °C over the 5 wt% Ni supported on Ce-10Cu-O, Ce-La-10Cu-O and Ce-Sm-10Cu-O carriers.  $\text{CH}_4$  conversions ( $X_{\text{CH}_4}$ , %)  $\sim 80\%$  are seen over the Ni/Ce-La-10Cu-O and Ni/Ce-Sm-10Cu-O catalysts but lower (ca. 65–72%) over Ni/Ce-10Cu-O. After 12 h TOS, lower  $X_{\text{CH}_4}$  (%) values than  $X_{\text{CO}_2}$  (%) were obtained for all three catalysts. This leads to  $\text{H}_2/\text{CO}$  gas product ratios slightly less than unity (0.8–0.95, Table 2). In the case of Ni/Ce-La-10Cu-O for short TOS (ca. 0.5 h), the  $\text{H}_2/\text{CO}$  ratio takes a value slightly higher than unity ( $\text{H}_2/\text{CO} = 1.1$ ). This behavior is attributed to competing side reactions that occur simultaneously with the DRM, such as the reverse water-gas shift reaction ( $\text{CO}_2 + \text{H}_2 \rightleftharpoons \text{CO} + \text{H}_2\text{O}$ ),  $\text{CH}_4$  decomposition ( $\text{CH}_4 \rightarrow \text{C} + 2\text{H}_2$ ), carbon oxidation to CO and

$\text{CO}_2$ , and steam methane reforming ( $\text{CH}_4 + \text{H}_2\text{O} \rightleftharpoons \text{CO} + 3\text{H}_2$ ) [87]. The  $X_{\text{CH}_4}$ ,  $X_{\text{CO}_2}$  and the  $\text{H}_2/\text{CO}$  gas product ratio values corresponding to *equilibrium* conditions for the DRM only, and for the reaction network consisting of both DRM and RWGS, are reported in Table 2 (values in parentheses). The equilibrium condition was investigated at  $P = 1$  atm,  $T = 750$  °C and with a  $\text{CH}_4/\text{CO}_2$  feed gas ratio equal to 1:1 using Aspen Plus software.  $\text{CO}_2$  and  $\text{CH}_4$  were chosen as the reactants, while the other components were CO, H<sub>2</sub> and H<sub>2</sub>O; an RGIBBS reactor was employed for the simulation.

In the case of  $\text{CH}_4$  conversion, the experimentally measured values were always lower than the equilibrium values either for DRM or DRM/RWGS for all three catalysts. On the other hand, the  $\text{CO}_2$  conversion for the Sm-doped ceria supported Ni was very similar to that corresponding to equilibrium for the DRM/RWGS network, whereas in the case of La-doped ceria supported Ni,  $\text{CO}_2$  conversion was lower than that corresponding to DRM or DRM/RWGS equilibrium condition. As shown in Table 2, the equilibrium value of  $\text{H}_2/\text{CO}$  gas product ratio for DRM alone is unity but becomes 0.92 after considering the DRM/RWGS reaction network.

The Sm<sup>3+</sup>-doped ceria supported Ni catalyst shows a  $\text{H}_2$ -yield of 58.2% after 12 h of reaction, larger by  $\sim 25\%$  compared to the La<sup>3+</sup>-doped ceria supported Ni (ca. 42.7%, Table 2), and both catalytic systems show practically no deactivation after 12 h of DRM. Of interest is the drop of  $\text{H}_2$ -yield by  $\sim 23\%$  in the case of La<sup>3+</sup>-doped ceria supported Ni after increasing the TOS from 0.5 to 12 h (Table 2). Given the fact that the  $X_{\text{CH}_4}$  remains constant, the  $X_{\text{CO}_2}$  increases but the CO-yield remains the same, it appears that RWGS and carbon oxidation to CO takes place between 0.5 and 12 h in DRM. This result might be linked to the significantly lower amount of carbon deposited after 12 h in DRM compared to the Sm<sup>3+</sup>-doped ceria supported Ni (1.5 vs 19.8  $\text{mg C g}^{-1}_{\text{cat}}$ , Table 2). Ni/Ce-10Cu-O catalyst, after 12 h in DRM, it showed the lowest activity,  $\text{H}_2$ -yield, and  $\text{H}_2/\text{CO}$  gas product ratio among all three catalysts.

The carbon accumulated after 12 h of DRM was measured by employing temperature-programmed oxidation (TPO). The use of La<sup>3+</sup>-doped ceria support substantially inhibited carbon accumulation (ca. 1.5  $\text{mg C g}_{\text{cat}}^{-1}$ ) when compared to the Cu-doped ceria (ca. 23.2  $\text{mg C g}_{\text{cat}}^{-1}$ ) and Sm<sup>3+</sup>-doped ceria (ca. 19.8  $\text{mg C g}_{\text{cat}}^{-1}$ ) (Fig. 8B, Table 2). The Cu-doped and Sm<sup>3+</sup>-doped ceria supported Ni accumulated 15.5- and 13.2-times higher amounts of carbon than La<sup>3+</sup>-doped counterpart. When the accumulated carbon (12 h in DRM) is normalised to the  $\text{H}_2$  product yield (Table 2, last column), the La-doped ceria supported Ni still exhibits 11.2 times lower amount of C per amount of  $\text{H}_2$  gas product per mass of catalyst ( $\text{mg C/mg H}_2/\text{g}_{\text{cat}}$ ).

The TPO- $\text{CO}_2$  traces of Ni/Ce-La-10Cu-O (Fig. 8B, b) and Ni/Ce-Sm-10Cu-O (Fig. 8B, c) catalysts have similar profiles, as opposed to the Ni/Ce-10Cu-O (Fig. 8B, a). As noted in the Experimental Section 2.5.1, a 20-

**Table 2**

Conversions of  $\text{CH}_4$  and  $\text{CO}_2$ ,  $\text{H}_2$ -yield (%), and  $\text{H}_2/\text{CO}$  gas product ratio after DRM at  $750$  °C (20%  $\text{CO}_2$ /20%  $\text{CH}_4/\text{He}$ ) for 0.5 h and 12 h on the 5 wt% Ni supported on Ce-M-10Cu-O (M = Sm or La) and Ce-10Cu-O carriers. The amount of carbon accumulated ( $\text{mg C g}^{-1}_{\text{cat}}$ ) after 12 h of DRM is also presented.

Catalyst	5 wt% Ni/Ce-M-10Cu-O	Time (h)	$X_{\text{CH}_4}$ (%)	$X_{\text{CO}_2}$ (%)	$\text{H}_2$ yield (%)	$\text{H}_2/\text{CO}$	$\text{mg C g}^{-1}_{\text{cat}}$
M = La	5 wt% Ni/Ce-10Cu-O	0.5	71.8 (86.6) <sup>a</sup> (83.6) <sup>b</sup>	78.4 (86.6) <sup>a</sup> (90.3) <sup>b</sup>	45	0.9 (1.0) <sup>a</sup> (0.92) <sup>b</sup>	n.d.
		12	65	73.3	41.3	0.8	23.2 (0.045) <sup>c</sup>
	M = Sm	0.5	80.3	76.4	55.3	1.05	n.d.
		12	80.8	81.4	42.7	0.85	1.5 (0.0025) <sup>c</sup>
M = Sm	5 wt% Ni/Ce-Sm-10Cu-O	0.5	81.2	89.7	60.5	0.95	n.d.
		12	81.4	89.6	58.2	0.95	19.8 (0.028) <sup>c</sup>

n.d.: not determined.

<sup>a</sup> Number in parentheses presents the estimated equilibrium conversions of  $\text{CH}_4$  and  $\text{CO}_2$  and the  $\text{H}_2/\text{CO}$  product gas ratio for the DRM alone; feed gas composition: 20 vol%  $\text{CH}_4$ /20 vol%  $\text{CO}_2$ /60 vol% He;  $T = 750$  °C.

<sup>b</sup> Number in parentheses presents the estimated equilibrium conversions of  $\text{CH}_4$  and  $\text{CO}_2$  and the  $\text{H}_2/\text{CO}$  gas product ratio when both the DRM and RWGS reactions consist the network of reactions; feed gas composition: 20 vol%  $\text{CH}_4$ /20 vol%  $\text{CO}_2$ /60 vol% He;  $T = 750$  °C.

<sup>c</sup> Number in parentheses indicates  $\text{mg C/mg H}_2/\text{g}_{\text{cat}}$ .

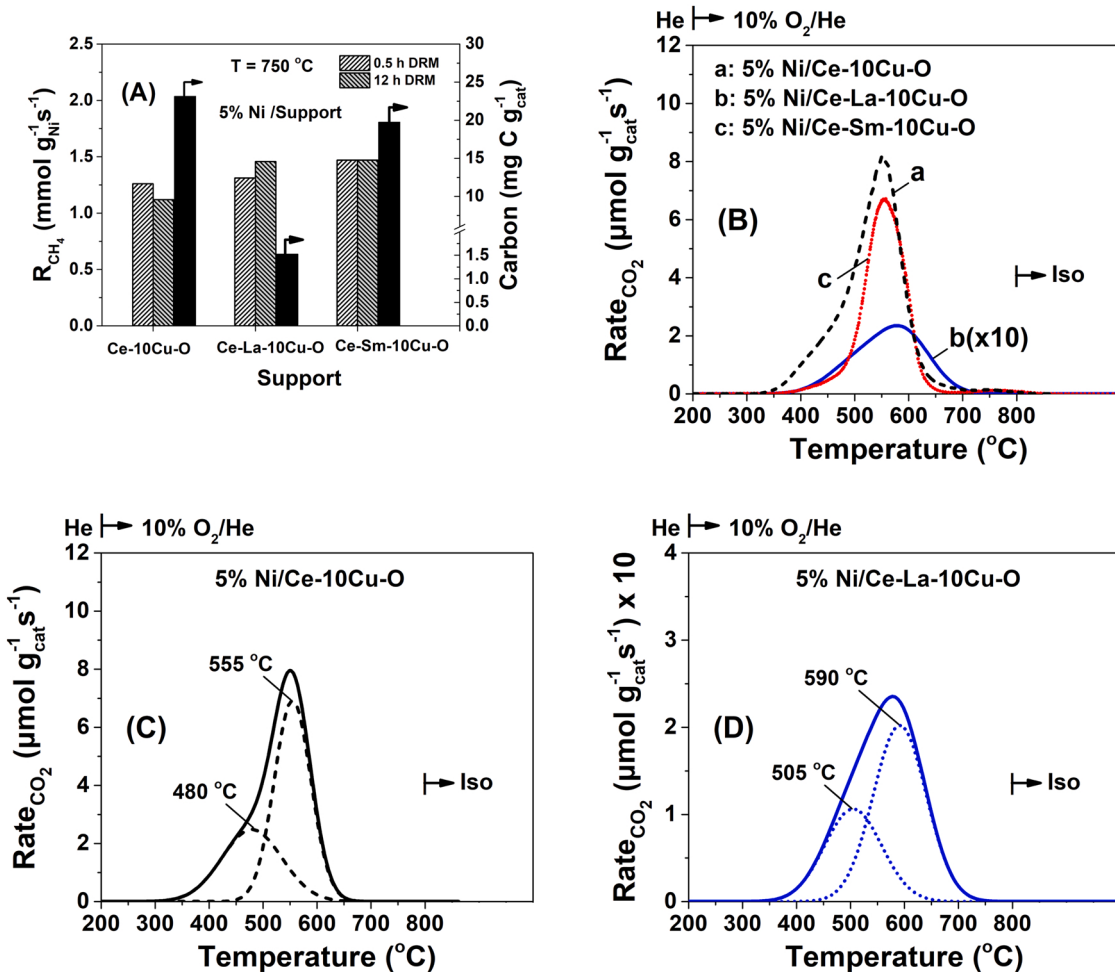


**Fig. 8.** (A) Integral rates ( $\text{mmol g}^{-1} \text{Ni s}^{-1}$ ) of  $\text{CH}_4$  conversion after 0.5 h and 12 h of DRM (20 vol%  $\text{CH}_4$ / 20%  $\text{CO}_2/\text{He}$ ) at  $750^\circ\text{C}$ , and amount of carbon accumulated after 12 h DRM; (B)  $\text{CO}_2$ -TPO traces of carbon oxidation after 12 h of DRM at  $750^\circ\text{C}$  over (a) 5 wt% Ni/Ce-10Cu-O, (b) 5 wt% Ni/Ce-La-10Cu-O and (c) 5 wt% Ni/Ce-Sm-10Cu-O catalysts. Deconvolution of TPO-CO<sub>2</sub> traces for the 5 wt% Ni/Ce-10Cu-O (C) and 5 wt% Ni/Ce-La-10Cu-O (D) catalysts.

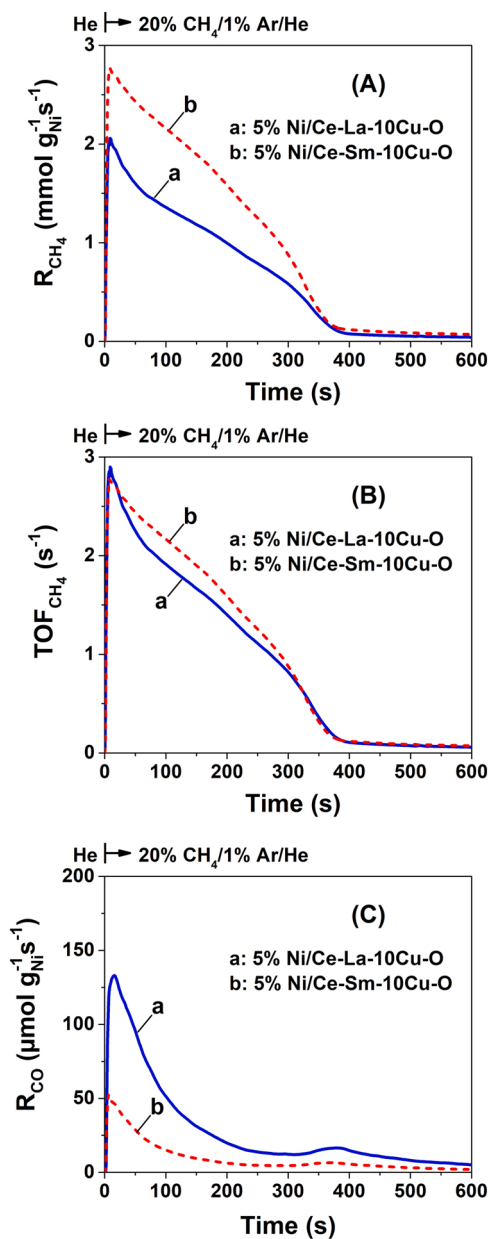
min He purge at  $750^\circ\text{C}$  and a temperature increase to  $800^\circ\text{C}$  in He gas flow, following DRM, were applied to ensure decomposition before TPO for possible presence of carbonates and/or formate species. The possibility that CO and/or  $\text{CO}_2$  might also be the result of oxidation of deposited carbon by the lattice oxygen of support under He thermal gas treatment cannot be excluded (see Section 3.9). Fig. S8A,B presents the transient response curves of CO and  $\text{CO}_2$  formation under the 20-min He gas treatment of the Ni/Ce-Sm-10Cu-O catalyst at  $750^\circ\text{C}$  and in the  $750$ – $800^\circ\text{C}$  range, respectively. The amount of CO and  $\text{CO}_2$  were found to be 115 and 11  $\mu\text{mol g}^{-1}$ , respectively, whereas only 6.8 and 0.65  $\mu\text{mol g}^{-1}$  under the He gas treatment in the  $750$ – $800^\circ\text{C}$  range. Considering that the amount of carbon estimated in TPO (Fig. 8B, trace c) was 1650  $\mu\text{mol g}^{-1}$ , underestimation of deposited carbon would be less than 8%, considering that all equivalent carbon removed by the He gas treatment was carbon derived during DRM; no carbonate/formate adsorbed species.

An attempt was made to deconvolute the TPO-CO<sub>2</sub> traces recorded over the Ni/Ce-10Cu-O (Fig. 8C) and Ni/Ce-La-10Cu-O (Fig. 8D) catalysts. It is seen that introduction of La<sup>3+</sup>-heteroatom in the Ce-10Cu-O support resulted in the accumulation of two types of carbon, similar to the case of Ce-10Cu-O but slightly less active in oxidation ( $T_M$  shifts to higher temperatures). The proportion of the two types of carbon (peak area ratio between low- and high-T peaks) was found to be also similar: 0.59 (Ce-10Cu-O) vs. 0.56 (Ce-La-10Cu-O). In the case of Ni/Ce-Sm-10Cu-O, one rather symmetrical peak ( $T_M \sim 550^\circ\text{C}$ ) was observed.

### 3.7. Transient methane decomposition reaction (20% $\text{CH}_4/\text{He}$ )

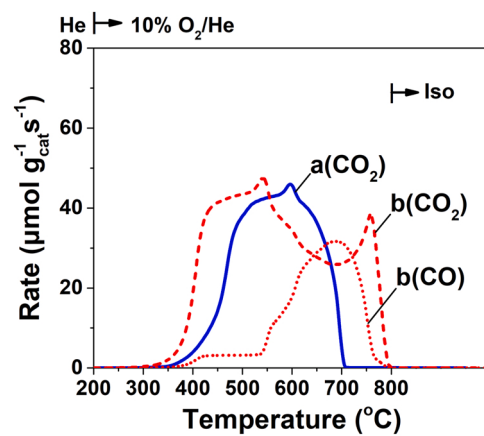
The transient kinetics of  $\text{CH}_4$  decomposition (20 vol%  $\text{CH}_4/\text{He}$ ) at  $750^\circ\text{C}$  was investigated for the Sm-doped and La-doped Ce-10Cu-O supported Ni catalysts based on which initial rates (on practically clean supported Ni surfaces) and the dynamics of carbon deposition, as well as the total amount of carbon accumulated after 30 min in  $\text{CH}_4/\text{He}$  were estimated. Fig. 9A and B presents the dynamic kinetic rate of  $\text{CH}_4$  decomposition per gram of Ni ( $\text{mmol g}^{-1} \text{Ni s}^{-1}$ ) and in terms of  $\text{TOF}_{\text{CH}_4} (\text{s}^{-1})$ , respectively, obtained after the step-gas concentration switch  $\text{He} \rightarrow 20$  vol%  $\text{CH}_4/1$  vol%  $\text{Ar}/\text{He}$  (t) at  $750^\circ\text{C}$  was applied over the Ni/Ce-La-10Cu-O (curve a) and Ni/Ce-Sm-10Cu-O (curve b) catalytic surfaces. There is a sharp increase in the rate, which should be considered as the *initial kinetic rate* of  $\text{CH}_4$  decomposition on a practically carbon-free Ni surface. The  $\text{TOF}_{\text{CH}_4} (\text{s}^{-1})$  vs time profile appears practically the same for the two supported Ni catalytic surfaces (Fig. 9B), as opposed to the rate expressed per unit mass of Ni metal, where for Ni/Ce-Sm-10Cu-O the initial rate is larger by  $\sim 35\%$  compared to Ni/Ce-La-10Cu-O (Fig. 9A). The initial rate of  $\text{CH}_4$  decomposition very quickly drops and takes a low value after  $\sim 7$  min on reaction stream for both catalysts, which continues to slowly decrease and vanishes after  $\sim 20$  min on reaction stream. The dynamics of  $\text{CH}_4$  decomposition, and thus of carbon deposition, presents similar features for the two catalytic surfaces, considering the shapes of the transient response curves obtained (Fig. 9A and B).

Fig. 9C shows the dynamic evolution of the rate of CO formation



**Fig. 9.** Transient rates of  $\text{CH}_4$  decomposition per mass of Ni ( $R_{\text{CH}_4}$ ,  $\text{mmol g}^{-1} \text{Ni s}^{-1}$ ) (A),  $\text{TOF}_{\text{CH}_4}$  ( $\text{s}^{-1}$ ) (B), and (C) transient rates of CO formation obtained after the switch  $\text{He} \rightarrow 20 \text{ vol\% CH}_4/1 \text{ vol\% Ar/He}$  ( $t$ ) at  $750^\circ\text{C}$  over (a) 5 wt%  $\text{Ni/Ce-La-10Cu-O}$  and (b) 5 wt%  $\text{Ni/Ce-Sm-10Cu-O}$  catalysts.  $W_{\text{cat}} = 20 \text{ mg} + 30 \text{ mg SiC}$ ;  $F_T = 50 \text{ mL min}^{-1}$ .

( $\mu\text{mol g}^{-1} \text{Ni s}^{-1}$ ) obtained at the same switch  $\text{He} \rightarrow 20 \text{ vol\% CH}_4/1 \text{ vol\% Ar/He}$  ( $t$ ). The formation of CO is clearly the result of carbon oxidation by the lattice oxygen of support, the carbon being produced after  $\text{CH}_4$  decomposition on the Ni surface. The same transient experiment conducted over the supports alone resulted in very small rates of CO formation and methane conversion. As shown in Fig. 9C, the initial kinetic rate of CO formation on the  $\text{La}^{3+}$ -doped ceria supported Ni is  $\sim 2.3$  times larger than on  $\text{Sm}^{3+}$ -doped ceria supported Ni, and larger throughout the transient. This is an important result since the formation of CO, as mentioned previously, is the result of the oxidation of carbon by lattice oxygen. As will be shown later by  $^{18}\text{O}$ -transient isotopic experiments (Section 3.9), this lattice oxygen participates in the formation of CO under DRM reaction conditions. Following the initial rate of CO formation, a large drop in the rate occurs after  $\sim 1$  min on reaction stream, while afterwards, up to  $\sim 10$  min on stream, a slow decay is seen



**Fig. 10.** Transient rates of CO and  $\text{CO}_2$  formation obtained during TPO of carbon formed after 30 min in 20 vol%  $\text{CH}_4/\text{He}$  reaction at  $750^\circ\text{C}$ . (a)  $\text{CO}_2$  trace obtained over 5 wt%  $\text{Ni/Ce-La-10Cu-O}$ ; (b)  $\text{CO}_2$  and CO traces obtained over the 5 wt%  $\text{Ni/Ce-Sm-10Cu-O}$  catalyst.

(Fig. 9C, a-b). In the case of  $\text{La}^{3+}$ -doped ceria supported Ni, a small peak after  $\sim 6$  min on reaction stream was recorded (Fig. 9C, a), which was originated by the presence of favorable conditions for carbon gasification, e.g., an increased rate of carbon or lattice oxygen diffusion towards the Ni-support interface. A similar feature was recently reported for the 5 wt%  $\text{Ni/Ce}_{0.8}\text{Ti}_{0.2}\text{O}_{2-\delta}$  catalyst [21] for the same transient experiment.

It is also important to note that even though the amount of carbon deposited with time in  $\text{CH}_4/\text{He}$  is larger on the  $\text{Sm}^{3+}$ -doped ceria supported Ni (Fig. 9A, b), the rates of CO formation show an opposite trend (Fig. 9C). Thus, the rate of surface lattice oxygen diffusion towards the metal-support interface, and likely the rate of carbon diffusion on the Ni metal surface to form CO, are faster on the  $\text{La}^{3+}$ -doped than  $\text{Sm}^{3+}$ -doped  $\text{Ce-10Cu-O}$  supported Ni catalyst.

Fig. 10 presents the transient rates of CO and  $\text{CO}_2$  formation obtained during TPO after 30 min of methane decomposition (20 vol%  $\text{CH}_4/\text{He}$ ) at  $750^\circ\text{C}$  on  $\text{Ni/Ce-La-10Cu-O}$  ( $\text{CO}_2$ , curve a) and  $\text{Ni/Ce-Sm-10Cu-O}$  (curves b,  $\text{CO}_2$  and CO). The  $\text{CO}_2$ -TPO traces in both catalysts exhibit largely different profiles (shape and position), indicating different kinetics of carbon oxidation and likely of carbon structures. The  $\text{CO}_2$ -TPO trace over  $\text{Ni/Ce-La-10Cu-O}$  shows only a single peak centered at  $\sim 600^\circ\text{C}$ , with a shoulder on its rising part, where all the deposited carbon reacted with oxygen below  $700^\circ\text{C}$ . On the other hand, the  $\text{CO}_2$ -TPO trace of  $\text{Ni/Ce-Sm-10Cu-O}$  resulted in both  $\text{CO}_2$  and CO traces (Fig. 10, curves b). The  $\text{CO}_2$  trace presents two carbon oxidation peaks at  $\sim 550$  and  $750^\circ\text{C}$ , and the CO trace starts at  $\sim 380^\circ\text{C}$  and forms a plateau in the  $380 - 540^\circ\text{C}$  range, followed by a large peak centered at  $\sim 700^\circ\text{C}$ . The exact nature of CO and  $\text{CO}_2$  formation mechanisms during oxidation of carbon materials (surface chemistry and reactivity of  $\text{sp}^2$ -hybridized carbon) is still of great debate [88]. The formation of  $\text{CO}_2$  at relatively low temperatures is a primary surface reaction product, and not the

**Table 3**

Quantity of  $\text{CH}_4$  converted,  $\text{H}_2$  and CO formed ( $\text{mmol g}^{-1} \text{cat}$ ), and ratio of  $\text{CO}/\text{CH}_4$  obtained after 30 min of  $\text{CH}_4$  decomposition (20 vol%  $\text{CH}_4/\text{He}$ ) at  $750^\circ\text{C}$  ( $\text{GHSV} = 30,000 \text{ h}^{-1}$ ). The amount of carbon accumulated ( $\text{mmol g}^{-1} \text{cat}$ ) was measured by TPO.

Catalyst	$\text{CH}_4$ converted (mmol $\text{g}^{-1} \text{cat}$ )	$\text{H}_2$ production (mmol $\text{g}^{-1} \text{cat}$ )	CO production (mmol $\text{g}^{-1} \text{cat}$ )	$\text{CO}/\text{CH}_4$	$\text{mmol C g}^{-1} \text{cat}$
5 wt% $\text{Ni/Ce-M-10Cu-O}$					
M = La	18.0	39.4	1.0	0.04	19.0 (228 mg $\text{g}^{-1} \text{cat}$ )
M = Sm	33.0	68.6	0.3	0.01	37.0 (445 mg $\text{g}^{-1} \text{cat}$ )

result of a likely homogeneous CO oxidation at higher temperatures [88]. The CO/CO<sub>2</sub> ratio depends on reaction conditions, and the type of carbon material (e.g., size and degree of ordering of graphene layers). The oxygen surface coverage becomes important, the latter being influenced by the temperature, oxygen pressure, and the edge-to-basal-plane sites in the graphene layer [88]. It was also reported that an interconversion between spectator's stable surface intermediates (C<sub>b</sub>-O) and reactive intermediates (C<sub>e</sub>-O) can take place; C<sub>b</sub> and C<sub>e</sub> are a basal-plane and an edge-site within the graphene layer [88].

Based on the above fundamental aspects of oxidation of carbon, and the fact that CNTs are formed over the present supported Ni catalysts after DRM (see Section 3.10), the formation of CO<sub>2</sub> only in the case of La-doped Ce-10Cu-O supported Ni (Fig. 10) might likely be the result of an increased oxygen surface coverage from the support in contact with the CNTs given its higher mobility compared to the Sm-doped ceria support. Based on the TPO results of Fig. 10, removal of carbon via the participation of lattice oxygen of support is favored on La-doped than Sm-doped Ce-10Cu-O supported Ni, in harmony with results of a more detailed analysis of the oxidation of carbon formed under DRM conditions to CO(g) by the lattice oxygen of support as opposed to that via the CO<sub>2</sub> activation route, to be presented and discussed in the following Section 3.9. Table 3 summarizes the quantities (mmol g<sup>-1</sup><sub>cat</sub>) of CH<sub>4</sub> converted, H<sub>2</sub> and CO formed, and carbon accumulated (mmol C g<sup>-1</sup><sub>cat</sub> or mg C g<sup>-1</sup><sub>cat</sub>) as measured by TPO over the two catalytic surfaces. The CO/CH<sub>4</sub> ratio after 30 min of methane decomposition is also reported. The amount of carbon accumulated over the Ni/Ce-La-10Cu-O was found to be 228 mg C g<sup>-1</sup><sub>cat</sub>, which is about half the amount over the Ni/Ce-Sm-10Cu-O catalyst (445 mg C g<sup>-1</sup><sub>cat</sub>). This result is in harmony with the amounts of carbon measured after 12 h in DRM (Table 2).

Additionally, the CO/CH<sub>4</sub> ratio provides a first indication of the extent of lattice oxygen participation towards the formation of CO (g). It is noted that this ratio is *four times larger* in the case of La<sup>3+</sup>-doped ceria supported Ni (Table 3), in full agreement with the significantly higher transient rates of CO formation depicted in Fig. 9C.

### 3.8. Transient CO disproportionation (CO/He) reaction

A similar step-gas concentration switch, He → 20% CO/1% Ar/He (750 °C, 30 min) to that of methane decomposition was conducted to strictly compare the transient kinetic rates of the two carbon deposition routes, and the evolution of carbon accumulation for the same feed gas composition and time on stream (30 min). The same TPO experimental procedure as in the case of CH<sub>4</sub> decomposition (Fig. 10) was applied. The transient rates of CO(g) conversion over the two catalytic surfaces are compared in Fig. 11A. The rate response curves pass through a maximum at very short times, ca. after 2–3 s of the introduction of CO in the reactor, for both catalysts, and they are of very similar shape. The transient conversion rate of CO becomes practically zero after ~15–20 s (Fig. 11A). It is seen that the *initial kinetic rate* of CO conversion for Ni/Ce-Sm-10Cu-O is ~3.5 times larger than for Ni/Ce-La-10Cu-O, and larger transient rates are obtained throughout the reaction period of CO disproportionation. Of interest is the fact that the transient rates at t<sub>max</sub> are significantly lower than those of CH<sub>4</sub> decomposition over both catalytic systems (compare Figs. 9A and 11A). These results may suggest increasing rates for the Boudouard reaction (CO<sub>2</sub> + C → 2 CO) over the Sm<sup>3+</sup>-doped ceria supported Ni catalyst during DRM. The dynamics of CH<sub>4</sub> decomposition and CO disproportionation reactions appear very different apparently because of the different individual kinetics for the given supported Ni surfaces.

The amount of carbon accumulated after 30 min in 20 vol% CO/He reaction over the Ni/Ce-Sm-10Cu-O catalyst was found to be 0.25 mmol C g<sup>-1</sup><sub>cat</sub> (3 mg C g<sup>-1</sup><sub>cat</sub>) compared to 0.1 mmol C g<sup>-1</sup><sub>cat</sub> (1.2 mg C g<sup>-1</sup><sub>cat</sub>) for the Ni/Ce-La-10Cu-O catalyst (Fig. 11B). Very similar in shape and position CO<sub>2</sub>-TPO traces were obtained for the two catalytic surfaces, with at least three types of carbon (see CO<sub>2</sub>-TPO traces, Fig. 11B) oxidized at temperatures lower than 700 °C; only a very small amount of carbon is oxidized to CO<sub>2</sub> in the 700–800 °C range. The amount of carbon accumulated appears significantly larger in the case of CH<sub>4</sub> decomposition (Fig. 10) than CO disproportionation over both catalytic surfaces for the same gas composition (20 vol%) and TOS (30 min). This might be used to suggest that CH<sub>4</sub> decomposition is the *dominant route of carbon formation* compared to the CO disproportionation in the DRM over the present catalytic surfaces. The shapes of the CO<sub>2</sub>-TPO traces after CH<sub>4</sub> decomposition (Fig. 10) are largely different than those obtained after CO disproportionation (Fig. 11B). This may suggest that different types of carbon were formed under the two reaction gas environments, governed also by different carbon oxidation kinetics, as previously discussed.

The origin of carbon accumulation (CH<sub>4</sub> vs CO<sub>2</sub> activation route) in the DRM over Ni supported on ceria-based carriers has been investigated quantitatively by *isotopic studies* (labelling one of the reactants with <sup>13</sup>C) combined with temperature-programmed oxidation (TPO) [15]. It was found that the %-contribution of each reaction path largely depends on the support chemical composition and reaction temperature [15], and not on the Ni particle size in the case of Ni/Ce<sub>1-x</sub>Ti<sub>x</sub>O<sub>2-δ</sub> (d<sub>Ni</sub> in the 22–45 nm range) [21]. For example, for the latter catalytic system, carbon accumulation after 30 min of DRM (5%<sup>13</sup>CO<sub>2</sub>/5%<sup>12</sup>CH<sub>4</sub>/He) was found to exclusively derive via methane decomposition [19,21]. On the other hand, in the case of DRM at 550 °C over 5 wt% Ni/Ce<sub>0.8</sub>Pr<sub>0.2</sub>O<sub>2-δ</sub> and 5 wt% Ni/Ce<sub>0.8</sub>Zr<sub>0.2</sub>O<sub>2-δ</sub>, the dominant route of carbon accumulation was the CO disproportionation reaction, while at 750 °C both routes had approximately equal contribution [16]. In a similar work, Vasiliades et al. [22] reported a very similar origin of carbon accumulation at 550 and 750 °C over a series of 5 wt% Ni/Ce<sub>1-x</sub>Pr<sub>x</sub>O<sub>2-δ</sub> (x = 0–0.8) catalysts of similar Ni particle size (28–32 nm). A significant effect of NiPt alloy

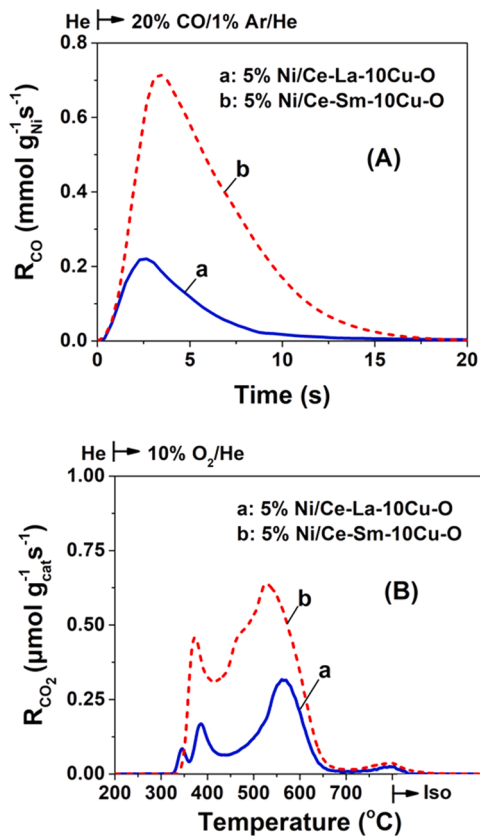


Fig. 11. (A) Transient rates (mmol g<sup>-1</sup><sub>Ni</sub> s<sup>-1</sup>) of CO conversion after the switch He → 20 vol% CO/1 vol% Ar/He at 750 °C. (B) CO<sub>2</sub>-TPO traces of carbon oxidation after 30 min in 20 vol% CO/He reaction at 750 °C over (a) 5 wt% Ni/Ce-La-10Cu-O and (b) 5 wt% Ni/Ce-Sm-10Cu-O catalysts. W<sub>cat</sub> = 0.02 g + 0.03 g SiC; F<sub>T</sub> = 50 mL min<sup>-1</sup>.

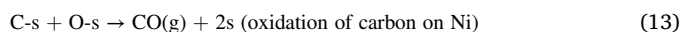
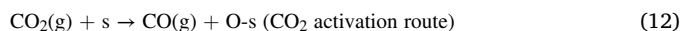
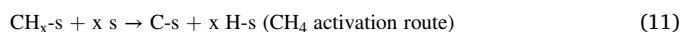
particles supported on  $\text{Ce}_{0.8}\text{Pr}_{0.2}\text{O}_{2-\delta}$  compared to the monometallic 5 wt% Ni was reported [20], where the presence of Pt increased the %-contribution of  $\text{CH}_4$  activation route for carbon accumulation; an increase from  $\sim 60\text{--}82\%$  ( $750\text{ }^\circ\text{C}$ , 5% $\text{CH}_4$ ,  $\text{CH}_4/\text{CO}_2 = 1$ ) was noticed.

### 3.9. Probing the oxidation of carbon by lattice oxygen of support during DRM

The participation of labile lattice oxygen of  $\text{Ce-La-10Cu-O}$  and  $\text{Ce-Sm-10Cu-O}$  supports in the oxidation of carbon derived during DRM on the Ni surface to form  $\text{CO(g)}$  (Eq. (5)) was probed following the experimental methodology described in Section 2.6. During the 15-min treatment of the catalyst at  $750\text{ }^\circ\text{C}$  with  $^{18}\text{O}_2/\text{Ar}$ , partial exchange of  $^{16}\text{O}$  for  $^{18}\text{O}$  in the solid (support surface and bulk) and oxidation of Ni to  $\text{Ni}^{18}\text{O}$  had occurred as depicted in Fig. S9. The dynamic rates of  $^{16}\text{O}_2$  and  $^{16}\text{O}^{18}\text{O}$  (Fig. S10A, B) were estimated [58], and after integration the amount of  $^{16}\text{O}$  exchanged for  $^{18}\text{O}$  in each catalyst was estimated. It is shown in Fig. S10 that the specific maximum  $^{16}\text{O}/^{18}\text{O}$  exchange rates,  $R^{\max}$  (per BET surface area or per gram of solid) recorded at the early stage of the transient over  $\text{Ni/Ce-La-10Cu-O}$  were larger by  $\sim 25\text{--}30\%$  compared to the corresponding ones over the Sm-doped supported Ni catalyst. The observed  $R^{\max}$  reflects the participation of surface-/subsurface lattice  $^{16}\text{O}$  of support, while larger times involve mainly the diffusion of bulk  $^{16}\text{O}$  within the lattice towards the surface (see  $R(^{16}\text{O}^{18}\text{O})$  transients, Fig. S10B). The shape and features of the transient curves of  $^{16}\text{O}^{18}\text{O}$  and  $^{16}\text{O}_2$  formation were similar for both solids, implying similar kinetics of surface and bulk oxygen diffusion and exchange [58]. The equivalent amount of  $^{18}\text{O}$  required to fully oxidize Ni to  $\text{Ni}^{18}\text{O}$  during the 15-min treatment of the catalyst with  $^{18}\text{O}_2/\text{Ar}$  at  $750\text{ }^\circ\text{C}$  was subtracted (0.85  $\text{mmol g}^{-1}$ ) from the total amount estimated. It was found that an amount of  $^{16}\text{O}$  larger by  $\sim 20\%$  was exchanged for the  $\text{La}^{3+}$ -doped ceria compared to the  $\text{Sm}^{3+}$ -doped ceria support alone (10.3 vs. 8.5  $\text{mmol}^{16}\text{O g}_{\text{cat}}^{-1}$ ).

The partial  $^{16}\text{O}/^{18}\text{O}$  exchange followed a quick ( $\sim 5$  min) cooling of reactor to  $400\text{ }^\circ\text{C}$  in the flow of  $^{18}\text{O}_2/\text{Ar}$  gas, and a subsequent reduction of the catalyst at  $400\text{ }^\circ\text{C}$  in pure  $\text{H}_2$  for 1 h to ensure reduction of  $\text{Ni}^{18}\text{O}$  (some  $\text{Ni}^{16}\text{O}$  reduction is not excluded) to  $\text{Ni}^0$  metal. At the same time, some small amount of  $^{18}\text{O}$  of support might have been removed, and this was assessed in a separate experiment (see Section 2.6), results of which are presented in Fig. S11. It is seen that both catalysts present not similar isothermal hydrogen reduction rate profiles (Fig. S11A). It was found that 0.9 (La-doped sample) and 0.8  $\text{mmol g}^{-1}$  of  $^{18}\text{O}$  (Sm-doped sample) were removed by  $\text{H}_2$  to form  $\text{H}_2^{18}\text{O}$  (Fig. S11B), which are less than 5% of available oxygen in pure ceria in its fully oxidized state. Following  $\text{H}_2$  reduction at  $400\text{ }^\circ\text{C}$ , the catalyst temperature was increased in He flow to  $750\text{ }^\circ\text{C}$  prior to the switch to the DRM gas mixture.

Fig. 12A and B presents the dynamic evolution of the  $\text{C}^{18}\text{O(g)}$  and  $\text{C}^{16}\text{O(g)}$  formation rates at the step-gas switch  $\text{He} \rightarrow 20\text{ vol\% CH}_4/20\text{ vol\% CO}_2/2\text{ vol\% Ar/He}$  ( $750\text{ }^\circ\text{C}$ ,  $t$ ), following  $^{16}\text{O}/^{18}\text{O}$  exchange at  $750\text{ }^\circ\text{C}$  and  $\text{H}_2$  reduction at  $400\text{ }^\circ\text{C}$ , for the two catalysts investigated, respectively. The  $\text{C}^{18}\text{O(g)}$  formation is due to the reaction between the lattice oxygen of support labelled  $^{18}\text{O}_{\text{L}}$  (after  $^{18}\text{O}/^{16}\text{O}$  exchange), and the  $^{12}\text{C}$  formed after the step-gas switch to the DRM reaction gas mixture (Eqs. (1) and (2)). The  $\text{C}^{16}\text{O(g)}$  transient response curve is due to the carbon oxidation by oxygen species derived from the  $\text{C}^{16}\text{O}_2$  activation route during DRM over the Ni surface, according to Eqs. (11)–(13) (s: surface Ni site).



It is observed that the shapes of the  $\text{C}^{18}\text{O(g)}$  dynamic rate response curves and the time of appearance of maximum,  $R^{\max}$  ( $\text{C}^{18}\text{O}$ ) (Fig. 12A, B) at  $t_m \sim 6\text{--}7\text{ s}$  are similar for both catalysts. On the other hand, the evolution of the rate of  $\text{C}^{16}\text{O}$  formation is slower over the La-doped

supported Ni compared to the Sm-doped one, where steady-state rate for the  $\text{C}^{16}\text{O(g)}$  formation is reached at  $\sim 75\text{ s}$  for the latter compared to  $t > 100\text{ s}$  for the former catalytic system. Eventually,  $\text{Ni/Ce-Sm-10Cu-O}$  reaches a slightly higher steady-state rate of  $\text{C}^{16}\text{O}$  formation (after 3 min of DRM) than the La-doped counterpart, in harmony with the catalytic performance results shown in Fig. 8A (after 30 min in DRM).

### (a) The important features of $\text{C}^{18}\text{O}$ and $\text{C}^{16}\text{O}$ transients (Fig. 12)

What is important to understand in these transient rate response curves shown in Fig. 12 is the effect of support composition on the relative magnitude of  $\text{C}^{18}\text{O}$  to  $\text{C}^{16}\text{O}$  formation rate *at the initial stage of the transient* since  $^{18}\text{O}$  in the support is continuously depleted and replenished by  $^{16}\text{O}$  ( $\text{CO}_2$  source). The following rate analysis concerns the comparison of  $R^{\max}$  ( $\text{C}^{18}\text{O}$ ) associated with the surface  $^{18}\text{O}$ -lattice oxygen of support, as previously discussed. The  $R^{\max}$  ( $\text{C}^{18}\text{O}$ ) takes the value of  $\sim 285$  and  $210\text{ }\mu\text{mol g}^{-1}\text{cat s}^{-1}$  for the  $\text{La}^{3+}$ -doped and  $\text{Sm}^{3+}$ -doped ceria supported Ni, respectively. A better fundamental understanding about these transient kinetic rate values can be obtained if the rate of  $\text{C}^{18}\text{O}$  formation is normalized per Ni particle. According to the Ni loading and the Ni mean particle size reported in Table 1, it was estimated that the ratio of Ni particles per gram of catalyst for the  $\text{Sm}^{3+}$ -doped to that of  $\text{La}^{3+}$ -doped ceria catalyst is 2.64. Given this value, the ratio of  $R^{\max}$  ( $\text{C}^{18}\text{O}$ ) for the  $\text{La}^{3+}$ -doped to that of  $\text{Sm}^{3+}$ -doped ceria supported Ni becomes  $\sim 3.6$ . This means that on the average, a Ni particle deposited on  $\text{La}^{3+}$ -doped ceria provides  $\sim 3.6$  times higher rate of  $\text{C}^{18}\text{O(g)}$  formation (*carbon oxidation by lattice oxygen of support*) compared to a Ni particle deposited on  $\text{Sm}^{3+}$ -doped ceria carrier. As a first approximation, the transient rate of  $\text{C}^{18}\text{O}$  formation normalized

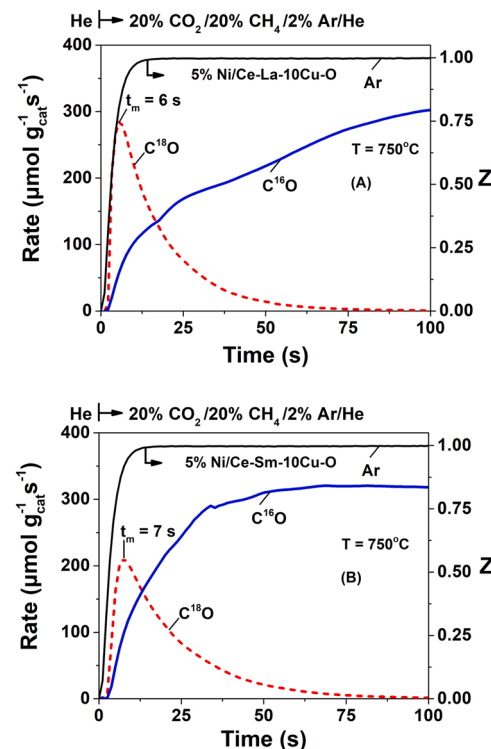


Fig. 12. Transient rates ( $\mu\text{mol g}^{-1}\text{s}^{-1}$ ) of  $\text{C}^{16}\text{O}$  and  $\text{C}^{18}\text{O}$  formation obtained during the switch  $\text{Ar} \rightarrow 20\text{ vol\% CH}_4/20\text{ vol\% CO}_2/2\text{ vol\% Ar/He}$  ( $t$ ) following  $^{16}\text{O}/^{18}\text{O}$  isotopic exchange at  $750\text{ }^\circ\text{C}$  and  $\text{H}_2$  reduction at  $400\text{ }^\circ\text{C}$  (see Section 2.6) over (A) 5 wt%  $\text{Ni/Ce-La-10Cu-O}$  and (B) 5 wt%  $\text{Ni/Ce-Sm-10Cu-O}$  catalysts. The dimensionless transient response,  $Z$  of Ar tracer is also shown.  $W_{\text{cat}} = 0.02\text{ g} + 0.03\text{ g SiC}$ ;  $F_T = 50\text{ mL min}^{-1}$ .

to the BET surface area,  $R(C^{18}O)$  ( $\mu\text{mol m}^{-2} \text{s}^{-1}$ ), can be described by the following Eq. (14):

$$\text{Rate (t)} = k C_c(t) C_{o-L}(t) \quad (14)$$

where,  $C_c(t)$  and  $C_{o-L}(t)$  are the time dependent local carbon and  $^{18}\text{O}$ -lattice oxygen concentrations ( $\mu\text{mol m}^{-2}$ ) established nearby the Ni particle-support interface during the  $\sim 75$  s transient, and  $k$  ( $\text{m}^2 \mu\text{mol}^{-1} \text{s}^{-1}$ ) is an average intrinsic site activity. Considering the ratio of the total length of perimeter of Ni particles ( $\text{cm g}_{\text{cat}}^{-1}$ ) for the  $\text{La}^{3+}$ -doped ceria to that of  $\text{Sm}^{3+}$ -doped ceria, a value of  $\sim 1.4$  was estimated. The ratio of the  $C_{o-L}(t)$  for the two solids at the time ( $t_{\text{max}}$ ) of appearance of  $R^{\text{max}}$  ( $C^{18}O$ ) was considered proportional to the ratio of the length of perimeters in the two Ni particles, and after assuming similar surface oxygen site density ( $\mu\text{mol O cm}^{-1}$ ), a value of  $\sim 1.4$  was obtained. To compare the local concentration of carbon,  $C_c(t)$ , we considered that the ratio in the amount of carbon accumulated for the two catalytic systems after 6–7 s of DRM is similar to that estimated after 12 h of DRM (Table 2, Fig. 12A and B), thus providing a value of  $\sim 13.2$ . Based on all the above, and after using Eq. (14) and considering the similar BET areas of the two solids, it was estimated that the rate constant,  $k$ , associated with the  $\text{La}^{3+}$ -doped ceria supported Ni particle is  $\sim 34$  times larger than that of  $\text{Sm}^{3+}$ -doped ceria supported Ni particle. This result agrees also with the relative initial transient rates of CO formation for the  $\text{CH}_4$  decomposition reaction shown in Fig. 9C, illustrating the significantly higher reactivity of lattice oxygen of  $\text{La}^{3+}$ -doped ceria supported Ni compared to the  $\text{Sm}^{3+}$ -doped counterpart for carbon gasification to  $\text{CO(g)}$ .

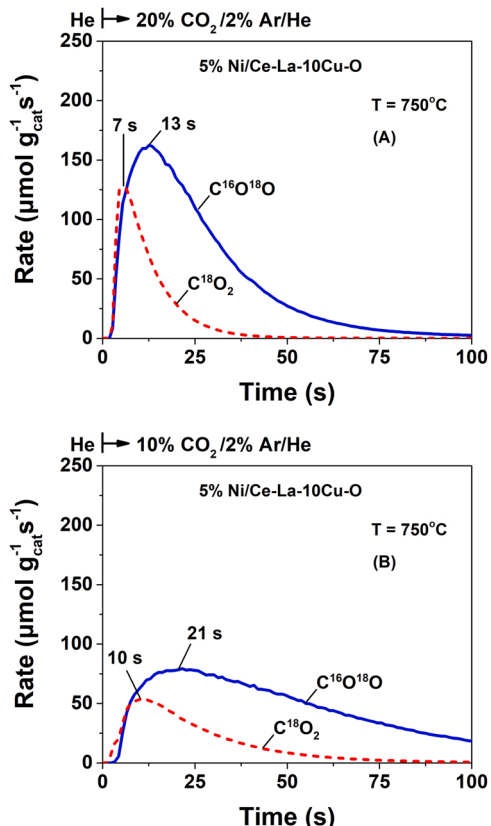


Fig. 13. Transient rates ( $\mu\text{mol g}^{-1} \text{cat s}^{-1}$ ) of  $\text{C}^{16}\text{O}^{18}\text{O}$  and  $\text{C}^{18}\text{O}_2$  formation obtained during the switch  $\text{He} \rightarrow x \text{ vol\% CO}_2/2 \text{ vol\% Ar/He}$  (t) ( $x = 20\%$  (A) and  $x = 10\%$  (B)), following  $^{16}\text{O}/^{18}\text{O}$  isotopic exchange at  $750^\circ\text{C}$  and  $\text{H}_2$  reduction at  $400^\circ\text{C}$  (Section 2.6) over the  $\text{Ni/Ce-La-10Cu-O}$  catalyst;  $W_{\text{cat}} = 0.02 \text{ g} + 0.03 \text{ g SiC}$ ;  $F_T = 50 \text{ mL min}^{-1}$ .

The relative comparison of the  $\text{C}^{18}\text{O(g)}$  and  $\text{C}^{16}\text{O(g)}$  transient rates at the *initial* period of the transient is a measure of the *relative contribution* of the two alternative routes of *carbon oxidation to CO formation*, namely, the classical DRM activation route (*Route 1*) described essentially by Eqs. (11)–(13), and *Route 2* (Eq. (5)), the participation of lattice oxygen of support. Since during the initial stage ( $t < 7 \text{ s}$ , Fig. 12) of the evolution of  $\text{C}^{18}\text{O}$  and  $\text{C}^{16}\text{O}$  formation rates the top surface atomic layer of the oxygen sub-lattice of support is practically fully labeled by  $^{18}\text{O}$ , in addition to several sub-surface oxygen layers as well, the initial rates estimated for  $\text{C}^{18}\text{O}$  and  $\text{C}^{16}\text{O}$  simulate the carbon and oxygen pools available during the initial DRM reaction conditions. Based on this rationale, the relative ratio  $R^{\text{max}}(\text{C}^{18}\text{O})/R(\text{C}^{16}\text{O})$  measured at the same time, e.g. 6–7 s (see Fig. 12A and B), is a valid *descriptor of the relative importance* of reaction Route 2 compared to reaction Route 1 operated under DRM to oxidize carbon (mainly derived from  $\text{CH}_4$  decomposition) to the desired  $\text{CO(g)}$  gas product. It is clearly seen in Fig. 12A and B that the present catalytic systems largely promote reaction Route 2, and further support is provided in what follows.

(b) Possibility of  $\text{C}^{16}\text{O}_2$  exchange with  $^{18}\text{O-L}$  followed by DRM The possibility that the transient rates of  $\text{C}^{18}\text{O(g)}$  formation (Fig. 12A and B) might also be the result of reforming of  $\text{CH}_4$  by  $\text{C}^{16}\text{O}^{18}\text{O}$  and  $\text{C}^{18}\text{O}_2$  formed after the exchange of  $^{16}\text{O}$  of  $\text{C}^{16}\text{O}_2$  for  $^{18}\text{O-L}$  of the support at the switch to the DRM gas mixture was examined. Fig. 13A and B presents the dynamic rates of  $\text{C}^{16}\text{O}^{18}\text{O}$  and  $\text{C}^{18}\text{O}_2$  formation ( $\mu\text{mol g}_{\text{cat}}^{-1} \text{s}^{-1}$ ) obtained at the switch  $\text{He} \rightarrow x \text{ vol\% CO}_2/2\text{Ar/He}$  (t) ( $x = 10$  (Fig. 13B) or  $20$  (Fig. 13A)) at  $750^\circ\text{C}$  following the 15-min  $^{16}\text{O}/^{18}\text{O}$  isotopic exchange at  $750^\circ\text{C}$  and similar gas treatments to those presented in Fig. 12A over the  $\text{Ni/Ce-La-10Cu-O}$  catalytic system. It is shown that the exchange of  $\text{C}^{16}\text{O}_2$  with  $^{18}\text{O-L}$  does occur with rate maxima for the  $\text{C}^{18}\text{O}_2$  formation at 7 and 10 s, and for the  $\text{C}^{16}\text{O}^{18}\text{O}$  formation at significantly longer times, ca. 13 and 21 s when  $20\% \text{CO}_2$  or  $10\% \text{CO}_2$  were used, respectively (Fig. 13A and B). Similar results were obtained for the  $\text{Ni/Ce-Sm-10Cu-O}$  catalytic system (Fig. S12).

Of importance was to compare the magnitude of the *maximum theoretical rate of  $\text{C}^{18}\text{O(g)}$  formation* that would have been obtained based on these exchange rates of  $^{18}\text{O}$ -containing  $\text{CO}_2$  species, if reforming of  $\text{CH}_4$  with the latter species *would immediately occur* producing  $\text{C}^{18}\text{O}/\text{H}_2$ . In particular, the early stage of the transient period at which a rate maximum in the  $\text{C}^{18}\text{O(g)}$  formation was recorded under DRM (ca. 6–7 s, Fig. 12) should be critically examined. At this point, it is very important to note that the dynamic evolution of  $\text{C}^{16}\text{O}^{18}\text{O}$  and  $\text{C}^{18}\text{O}_2$  rate response curves appear approximately proportional to the concentration of  $\text{CO}_2$  in the gas-phase (compare  $R_{\text{max}}$  in Fig. 13A and B). Furthermore, we should consider the fact that based on the  $Z_{\text{Ar}}(t)$  response shown in Fig. 12A and B, at times less than  $t_m$  (ca. 6–7 s), the concentration of  $\text{CO}_2$  exiting the reactor would be *less than 10 vol%* ( $Z < 0.5$ ) if no reaction/adsorption occurs. From this point of view, the exchange rates of gaseous  $\text{CO}_2$  with  $^{18}\text{O}$ -surface lattice oxygen at the initial stage of the transient should be compared favorably (less extent of exchange) to those depicted in Fig. 13B.

Fig. 14A and B compares the transient rate of  $\text{C}^{18}\text{O(g)}$  measured at the switch to the DRM gas mixture (curve a) with the theoretical  $\text{C}^{18}\text{O(g)}$  transient curve computed based on the transient rates of  $\text{C}^{16}\text{O}^{18}\text{O}$  and  $\text{C}^{18}\text{O}_2$  measured at the switch to the  $20\% \text{CO}_2/2\text{Ar/He}$  (curve b) and  $10\% \text{CO}_2/2\text{Ar/He}$  (curve c) gas mixture and when considering at the same time that *all  $\text{C}^{16}\text{O}^{18}\text{O}$  and  $\text{C}^{18}\text{O}_2$  formed participated exclusively to the reforming of  $\text{CH}_4$* . This comparison is made for the initial stage of the transient (0–25 s), where rate maxima for  $\text{C}^{18}\text{O(g)}$  at the switch to the DRM gas mixture (Fig. 12A and B) are of interest. Two important features from these transient  $\text{C}^{18}\text{O(g)}$  response curves (Fig. 14) must be discussed. First, there is a clear *time delay* in the

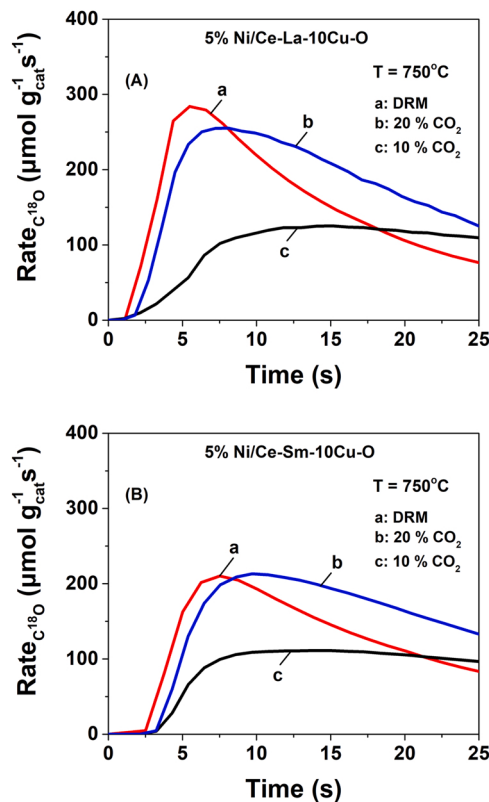


**Fig. 14.** Comparison of dynamic rates ( $\mu\text{mol g}^{-1}\text{cat s}^{-1}$ ) of  $\text{C}^{18}\text{O}$  formation obtained during the switch  $\text{Ar} \rightarrow 20\% \text{CH}_4/20\% \text{CO}_2/2\% \text{Ar}/\text{He}$  (t) (curve a), and that of theoretical  $\text{C}^{18}\text{O}$  formation if all  $\text{C}^{16}\text{O}^{18}\text{O}$  and  $\text{C}^{18}\text{O}_2$  obtained during the  $\text{Ar} \rightarrow 20\% \text{CO}_2/2\% \text{Ar}/\text{He}$  (t) (curve b), and  $\text{Ar} \rightarrow 10\% \text{CO}_2/2\% \text{Ar}/\text{He}$  (t) (curve c) switches participate in the DRM. (A) 5 wt% Ni/Ce-La-10Cu-O, and (B) 5 wt% Ni/Ce-Sm-10Cu-O catalyst.  $W_{\text{cat}} = 0.02 \text{ g} + 0.03 \text{ g SiC}$ ;  $F_T = 50 \text{ mL min}^{-1}$ .

appearance of the  $\text{C}^{18}\text{O}(\text{g})$  transient response arising from the exchange of  $\text{C}^{16}\text{O}_2$  with  $^{18}\text{O}_{\text{L}}$  followed by DRM (curves b, c) when compared to the experimentally measured  $\text{C}^{18}\text{O}$  response (curve a; after the switch to the DRM gas mixture). Secondly, for the Ni/Ce-La-10Cu-O, the measured  $\text{C}^{18}\text{O}$  rate formation value (curve a) at  $t_{\text{max}}$  (5 s) is larger by  $\sim 1.35$  and  $4.9$  times compared to the theoretical one that is associated with the exchange of  $^{18}\text{O}_{\text{L}}$  with 20 vol%  $\text{CO}_2$  (curve b) or 10%  $\text{CO}_2$  (curve c), respectively.

To further demonstrate that the initial rates of  $\text{C}^{18}\text{O}$  formation are largely due to the *fast gasification of carbon by surface lattice  $^{18}\text{O}$  of support*, the following are noted with emphasis:

- After 100 s of the switch to the DRM gas mixture (Fig. 12), the  $\text{CO}_2$  concentration at the exit of reactor is  $\sim 8$  vol% ( $X_{\text{CO}_2} = 60\%$ ). This implies that at times less than 6–7 s, the concentration of  $\text{CO}_2$  throughout the catalytic bed was less than 4 vol% ( $Z_{\text{Ar}} < 0.5$ , as discussed above).
- The rates of exchange of  $^{18}\text{O}_{\text{L}}$  with  $\text{CO}_2$  are reduced approximately proportional to the gaseous concentration of  $\text{CO}_2$  (compare Fig. 13A and B), and
- The transient rates of  $\text{C}^{16}\text{O}^{18}\text{O}$  and  $\text{C}^{18}\text{O}_2$  are *shifted towards higher times* when the feed gas  $\text{CO}_2$  concentration is reduced (see  $t_m$  values marked in Fig. 13A and B).

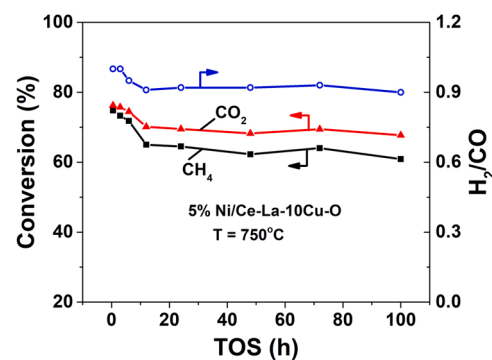


**Fig. 15.** Dry Reforming of Methane stability test (100 h) over the 5 wt% Ni/Ce-La-10Cu-O catalyst.  $T = 750^\circ\text{C}$ , 40%  $\text{CH}_4$ /40%  $\text{CO}_2$ /20%  $\text{He}$ , GHSV  $\sim 30,000 \text{ h}^{-1}$ .

Based on the transient  $\text{C}^{18}\text{O}(\text{g})$  formation rates shown in Fig. 12, the rate analysis presented in Fig. 14, and the offered discussion, the contribution of  $\text{C}^{16}\text{O}^{18}\text{O}$  and  $\text{C}^{18}\text{O}_2$  to the *initial  $\text{C}^{18}\text{O}(\text{g})$  transient response* at the switch to the DRM gas mixture must be considered very small. We have, therefore, illustrated in a *quantitative manner* the very important step of *carbon oxidation by labile oxygen of support* (Eq. (5)), which occurs very likely to a large extent at the metal-support interface. The rate of this reaction path appears larger than that of carbon oxidation by oxygen species provided by the  $\text{CO}_2$  activation route. The higher the rate of the former route the lower the amount of carbon accumulated at the critical initial stage of DRM, result that would prevent carbon transformation reactions to various inactive forms with increasing TOS in DRM. As presented and discussed in Section 3.2, NiCu alloy nanoparticles were formed after reduction of Ni/Ce-La(Sm)–10Cu-O catalyst with  $\text{H}_2$  at  $750^\circ\text{C}$  before DRM. In a recent experimental and DFT investigation on the effect of Cu addition to Ni/Al<sub>2</sub>O<sub>3</sub> for DRM [89], it was reported that an optimum Ni<sub>8</sub>Cu<sub>1</sub> alloy composition (slab model) suppressed carbon formation via  $\text{CH}_4$  decomposition due to a significant increase in the energy barrier for CH dissociation to C and H (major contributor of carbon). Furthermore, the adsorption energy of atomic C on monometallic Ni (111) surface was found to be larger compared to various fractional ML (monolayers) of Cu in the Ni/Cu (111) surface [89]. The latter is important since surface carbon diffusion on the NiCu alloy particle towards the interface (supported NiCu alloy particles) should be expected to proceed with a higher rate. Song et al. [90] have recently reported that the catalytic activity and stability were significantly affected by the NiCu alloy composition for the NiCu/Mg-Al-O catalyst tested for DRM at  $600^\circ\text{C}$ . They proposed that the decrease in the rate of  $\text{CH}_4$  decomposition and the increase of  $\text{CO}_2$  dissociation rate on Cu active sites were responsible for the suppression of coke deposition. In the present work, quantification of NiCu alloy phase developed on the fresh Ni/Ce-La(Sm)–10Cu-O catalytic systems was not attempted, but it seems logical to suggest that the existence of this phase seems to have played a positive role in the suppression of initial  $\text{CH}_4$  dissociation rate per gram basis reported in Fig. 9, and in the increase of initial rate of carbon gasification by lattice oxygen (Fig. 12A). The latter is envisioned via an increased diffusion rate of atomic carbon on the NiCu alloy particles towards the metal-support interface compared to monometallic Ni particles.

In a recent work on the effect of Ni particle size ( $d_{\text{Ni}} = 22\text{--}45 \text{ nm}$ ) on the carbon paths of DRM over Ni/Ce<sub>0.8</sub>Ti<sub>0.2</sub>O<sub>2.8</sub> catalyst, Efthathiou and his group [21] have demonstrated that when  $d_{\text{Ni}}$  (nm) becomes larger than a given size, even though the initial rate of oxidation of deposited carbon by lattice oxygen increases with  $d_{\text{Ni}}$  (ca. 22–45 nm), the rate of carbon polymerization on the Ni surface to form CNFs, graphite and

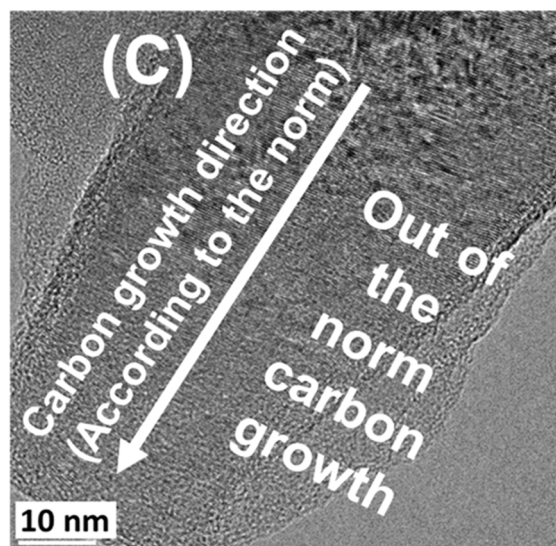
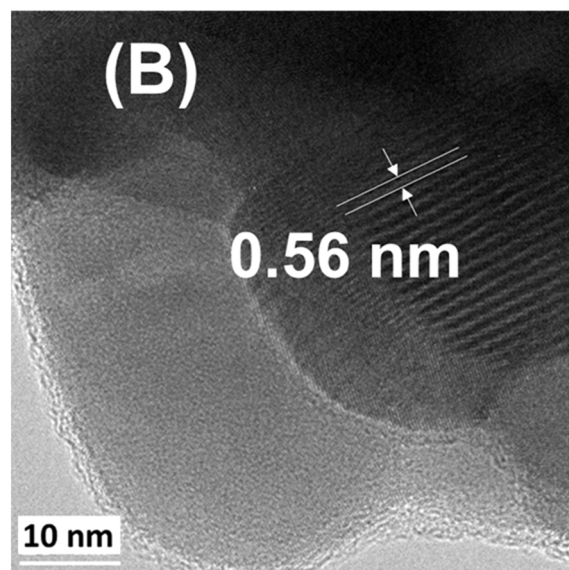
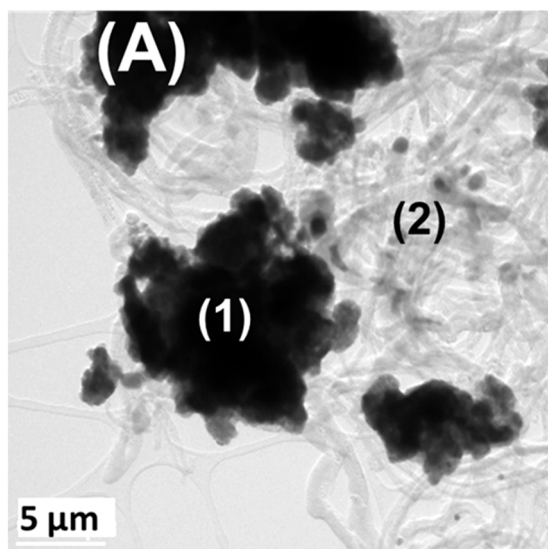
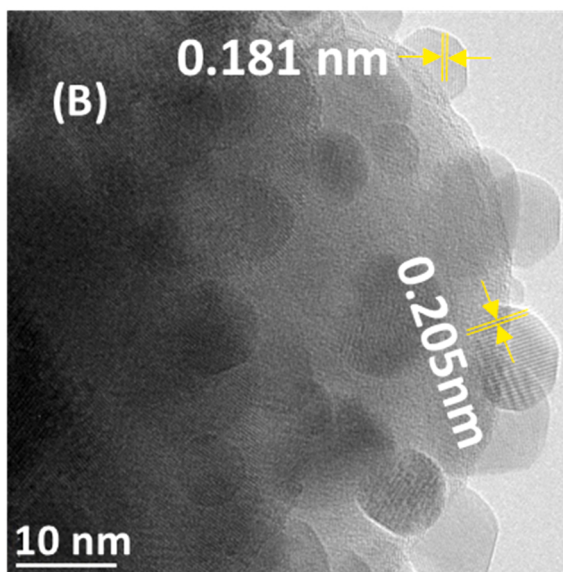
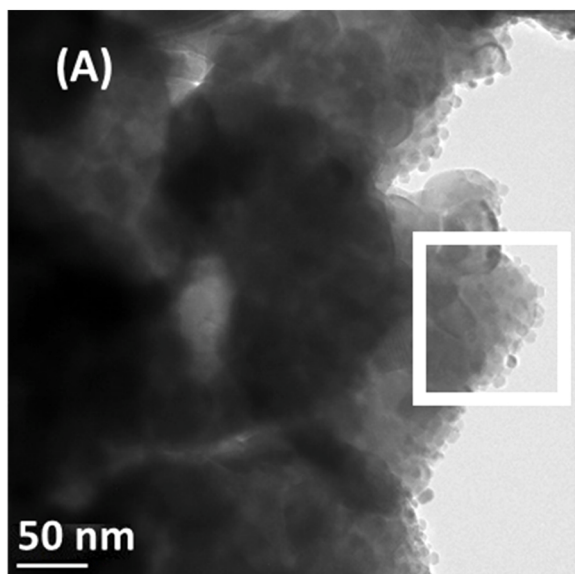


**Fig. 16.** (A) TEM image of the spent (100 h in DRM) Ni/Ce-La-10Cu-O catalyst, where the carbon-poor area (region 2) is marked. (B) zoomed part of TEM image (A) with Cu d-spacings indicated (0.181 and 0.205 nm).

amorphous carbon becomes more important with increasing  $d_{Ni}$  (nm) than the rate of carbon diffusion towards the Ni-support interface, followed by oxidation to CO. Thus, larger Ni particles (ca. 45 nm) accumulated significantly larger amounts of carbon than smaller Ni particles (ca. 22 nm) [21].

The present transient kinetic and isotopic experiments pave the way to better understand the role of heteroatoms introduced in the ceria lattice and used as carriers of Ni nanoparticles towards an efficient design of *carbon-resistant doped-ceria supported Ni catalysts* for future robust DRM catalytic technology.

### 3.10. Stability test – HRTEM studies over the spent Ni/Ce-La-10Cu-O catalyst

#### 3.10.1. Stability test

The 5 wt% Ni/Ce-La-10Cu-O DRM catalyst that showed significant reduction in the rate of carbon deposition after 12 h in DRM (20%CH<sub>4</sub> and CH<sub>4</sub>/CO<sub>2</sub> = 1, Fig. 8A) and small drop in activity compared to the

**Fig. 17.** (A) Ni/Ce-La-10Cu-O (spots 1, 2) surrounded by carbon nanotube (CNT) formation (region 1). (B) carbon encapsulation, and (C) CNT growth direction (opposite to the norm) over the 5 wt% Ni/Ce-La-10Cu-O after 100 h in DRM at 750 °C.

Sm-doped counterpart was further evaluated for long TOS using a reaction feed gas composition simulating potential applications of DRM (e.g., biogas and natural gas rich in CO<sub>2</sub>, namely, 40 vol% CH<sub>4</sub> and CH<sub>4</sub>/CO<sub>2</sub> = 1). The obtained stability test for 100 h TOS at 750 °C and GHSV of 30,000 h<sup>-1</sup> is presented in Fig. 15. Initial conversion values for both CH<sub>4</sub> and CO<sub>2</sub> of ~ 76% were recorded (86% equilibrium values for DRM alone), which drop to 61% and 68%, respectively, after 100 h of DRM. However, most of the drop of DRM activity occurred within the first 10 h of reaction. A stable H<sub>2</sub>/CO gas product ratio of ~ 0.9 in the 20–100 h TOS period was observed. The amount of carbon accumulated after the 100-h stability test was determined by TPO, and results are presented in Fig. S13. An amount of 235 mg C g<sup>-1</sup><sub>cat</sub> (or 23.5 wt%) corresponding to an average rate of 2.35 mg C g<sup>-1</sup><sub>cat</sub> h<sup>-1</sup> for carbon deposition was estimated.

### 3.10.2. HR-TEM studies over the aged Ni/Ce-La-10Cu-O catalyst

HR-TEM images of the Ni/Ce-La-10Cu-O catalyst after 100 h in DRM are presented in Fig. 16A, where carbon deposition can be clearly identified. The spent catalyst surface showed two regions, a carbon-poor one marked in Fig. 16A, and which is dominated by the formation of metallic Cu nanoparticles as shown in Fig. 16B, where fringes at 0.205 nm and 0.181 nm corresponding to metallic Cu (111) and (200), respectively, can be seen. Fig. 17A shows two marked locations illustrating encapsulation of the catalyst with carbon (carbon-rich, region 1), and carbon nanotubes (CNTs) formation (carbon-poor, region 2). Fig. 17B shows CNT of 0.56 nm diameter, which corresponds to a single-wall CNT grown on Cu particles [91,92]. The fringes possibly correspond to Moiré type fringes in Cu-SWCNT [22,24,27,31–34,91,92]. Some of the CNTs formed showed an opposite growth direction of the walls [93], as shown in the TEM image of Fig. 17C.

HR-TEM images showed that carbon-poor area (region 2) is populated with NiCu bimetallic alloy particles. The bimetallic alloy formation was seen also in the fresh catalyst (following calcination and H<sub>2</sub> reduction at 750 °C, Section 3.2), and reasons for its formation were previously discussed. The STEM-RGB mapping of the spent catalyst (Fig. S14A, B) shows the presence of NiCu alloy (cyan particles as the result of thorough mixing of green (Cu) and blue (Ni)). It must be pointed out that Cu particles (see Fig. 16B and Fig. S14B) can also be formed through a NiCu de-alloying. This route however is highly unlikely to occur due to the affinity/stability of the two constituents in the alloy (fcc structure, similar electronegativity, and atomic radius) compared to the counterpart oxide environment. These areas did not experience coking (Fig. 16B and Fig. S6A). A simplified illustration of the formation path of the two C-rich and C-poor regions (Fig. 17A) is attempted in Fig. S15.

In the EELS spectrum shown in Fig. S14C (spent catalyst), the white line peaks at ~ 855 and 872 eV represent Ni L<sub>3</sub> and L<sub>2</sub> absorption edges, respectively, and those at ~ 931 and 951 eV represent Cu L<sub>3</sub> and L<sub>2</sub> absorption edges, respectively [68]. EELS is sensitive to the electronic structure around the atoms, so it is used to determine the oxidation

states of Ni and Cu (based on L<sub>3</sub>/L<sub>2</sub> ratio) [68,94,95]. The estimation of this ratio, though, is difficult due to the presence of La and Ce in the present catalytic materials. Additionally, the formation of Cu<sup>0</sup> (in addition to NiCu alloy) on the surface of the spent Ni/Ce-La-10Cu-O catalyst, following 100 h of DRM, not seen in the case of fresh Ni/Ce-La-10Cu-O catalyst, could be linked to the presence of stronger CO/H<sub>2</sub> than H<sub>2</sub> gas reducing environment under DRM reaction conditions.

### 3.11. Carbon resistance of 5 wt% Ni/Ce-M-10Cu-O (M = La or Sm) DRM catalysts

The present ceria-based supported Ni (5 wt%) catalysts were compared with several other ceria-based supported Ni catalysts (monometallic and bimetallic Ni) reported in the literature [19,20,29, 96–98] and which were tested under very similar DRM reaction conditions (750 °C, feed gas composition, and TOS ≥ 12 h). The comparison is focused on their coke resistance (carbon deposition rate, and amount of carbon for given TOS, Table 4). The rate of carbon accumulation varies in the ~ 0.03– 3 mg g<sub>cat</sub><sup>-1</sup> h<sup>-1</sup> range, and the present 5 wt% Ni/45Ce-45La-10Cu-O compares favorably, ca. 0.125 mg C g<sub>cat</sub><sup>-1</sup> h<sup>-1</sup>. Some of the parameters that can be of critical importance are briefly discussed below.

- (a) The *synthesis method of support* and the method of *metal deposition* both regulate the development of metal-support interactions and the metal crystallite size/shape. It can be noticed that Ni/Ce-La-10Cu-O exhibits significantly better behavior compared to pure ceria-supported NiPt and NiCo catalysts of the same or higher total metal loading. This may lead to the conclusion that not only the metal nanoparticles intimacy drives the DRM reaction, but also the support composition (lattice oxygen mobility, surface basicity)/particle size [21], and the method of introduction of metal active sites on the catalyst surface.
- (b) The *active metal composition* shows a precedence when combined with a reducible support. For example, the enhanced coke resistance reported for the 5 wt% Ni/Ce<sub>0.8</sub>Ti<sub>0.2</sub>O<sub>2-δ</sub> [19] and 5 wt% Ni-0.5 wt% Pt/Ce<sub>0.8</sub>Pr<sub>0.2</sub>O<sub>2-δ</sub> [20] is due to metal-support synergistic interactions, and the ensemble metal size control in the bimetallic active sites through the incorporation of noble metal (Pt) reduces carbon formation rates and lowers the binding energy of carbon with metal sites. A similar effect was operated for the supported NiCu alloy nanoparticles present in the Ni/Ce-La-10Cu-O catalytic system.
- (c) The *active labile oxygen of support*. The lower rates of carbon accumulation seen in the 5 wt% Ni/Ce<sub>0.8</sub>Ti<sub>0.2</sub>O<sub>2-δ</sub> compared to 5 wt% Ni/Ce-La-10Cu-O (very similar Ni particle size) is related with the higher reactivity of surface lattice oxygen towards carbon, as evidenced by the transient isotopic experiments (Section 3.9), and the higher lattice oxygen mobility in Ti<sup>4+</sup>- than La<sup>3+</sup>- or

Table 4

Amount and rate of carbon accumulation after DRM (CH<sub>4</sub> = 20 vol%; CH<sub>4</sub>/CO<sub>2</sub> = 1; T = 750 °C) over various ceria-based supported Ni or Ni bimetallic catalysts.

Catalyst	CH <sub>4</sub> :CO <sub>2</sub> vol %/vol%	T (°C)	GHSV (L g <sub>cat</sub> <sup>-1</sup> h <sup>-1</sup> )	TOS (h)	carbon deposition (mg g <sub>cat</sub> <sup>-1</sup> )	Rate of carbon deposition (mg g <sub>cat</sub> <sup>-1</sup> h <sup>-1</sup> )	Ref.
5 wt% Ni/CeO <sub>2</sub>	20/20	750	30	12	30.7	2.56	[29]
5 wt% Ni/Ce-La-10Cu-O	20/20	750	30	12	1.5	0.125	This Work
5 wt% Ni/ Ce-Sm-10Cu-O	20/20	750	30	12	19.8	1.65	This Work
5 wt% Ni-0.5 wt% Pt/ Ce <sub>0.8</sub> Pr <sub>0.2</sub> O <sub>2-δ</sub>	20/20	750	60	12	1.3	0.108	[21]
3.75 wt% Co-3.75 wt% Ni/ CeO <sub>2</sub>	20/20	750	30	20	60	3	[96]
5 wt% Ni/ Ce <sub>0.8</sub> Ti <sub>0.2</sub> O <sub>2-δ</sub>	20/20	750	30	12	0.35	0.029	[19]
15 wt% Ni/MgO-Ce <sub>0.8</sub> Zr <sub>0.2</sub> O <sub>2</sub>	20/20	800	4.8 x 10 <sup>4</sup> h <sup>-1</sup>	40	~ 0	~ 0	[98]
3.6 wt% Ni-1.4 wt% Pt/CeO <sub>2</sub>	10/10	750	120	24	7.5	0.31	[97]

Sm<sup>3+</sup>-doped ceria support that affects at least initial rates of carbon oxidation.

Based on the above remarks, reduction in the rate of carbon accumulation for the Ni/45Ce-45La-10Cu-O catalyst can be tailored/optimized (keeping the activity high) with the presence of other bimetallic active sites (e.g., NiCu, NiPt, NiCo, NiRu), and/or tuned for optimal Ni particle size [21] by adopting a controlled deposition method. The 15 wt % Ni/MgO-Ce<sub>0.8</sub>Zr<sub>0.2</sub>O<sub>2</sub> [98] tested at 800 °C for 40 h was reported to present practically zero carbon accumulation (Table 4). It should be noted, however, that three times larger Ni loading and a higher reaction T (ca. 800 °C) for which carbon accumulation is expected to be lower were used [98].

#### 4. Conclusions

Introduction of La<sup>3+</sup> and Sm<sup>3+</sup> (40 at%) into Cu-doped ceria (Ce-10Cu-O) by an enhanced microwave approach synthesis presented tuned intrinsic properties, such as redox behavior (H<sub>2</sub>-TPR studies), surface basicity (CO<sub>2</sub>-TPD studies), and lattice oxygen mobility (<sup>16</sup>O/<sup>18</sup>O transient isotopic exchange), while maintaining the cubic fluorite structure with some MO<sub>8</sub> (M = La, Sm) impurity micro-phases present (PXRD, Raman studies). The Sm<sup>3+</sup> heteroatom has increased the total surface concentration of basic sites and those of medium and strong strength compared to the La<sup>3+</sup> heteroatom. On the contrary, La<sup>3+</sup> heteroatom has increased the mobility of surface/subsurface lattice oxygen. When both Ce-La-10Cu-O and Ce-Sm-10Cu-O were used as carriers of 5 wt% Ni, after calcination (20%O<sub>2</sub>/He) and reduction by hydrogen at 750 °C, the formation of NiCu alloy nanoparticles was observed (HRTEM, STEM/EDX, RGB mapping analysis) along with Ni nanoparticles in the 18–24 nm range.

After 12 h of DRM (20%CH<sub>4</sub>, CH<sub>4</sub>/CO<sub>2</sub> = 1) at 750 °C, the La<sup>3+</sup>-based doped ceria supported Ni presented an average rate of carbon accumulation lower by ~ 13 times compared to the Sm<sup>3+</sup>-based doped ceria supported Ni (e.g., 1.5 mg C g<sup>-1</sup>cat and 19.8 C g<sup>-1</sup>cat), respectively. This effect was linked to the larger mobility of surface/subsurface lattice oxygen of La<sup>3+</sup>-based doped ceria support that facilitated faster removal of carbon formed on the Ni and NiCu surfaces during the initial DRM reaction towards CO(g) formation, as evidenced by transient <sup>16</sup>O/<sup>18</sup>O isotopic exchange experiments followed by DRM. Both Ni/Ce-La(Sm)-10Cu-O catalytic systems presented enhanced initial rates of oxidation of carbon by surface lattice oxygen of support at the Ni-support interface, the former derived via CH<sub>4</sub> decomposition during DRM, compared to those obtained by the participation of atomic oxygen derived from the CO<sub>2</sub> activation route. After the interfacial lattice O is consumed, it is replenished following CO<sub>2</sub> dissociation on the oxygen vacant sites of support. It was found that the initial kinetic rate of disproportionation reaction (2 CO → CO<sub>2</sub> + C) is fast as well but lower by a factor of ~ 10 and ~ 4 with respect to that of CH<sub>4</sub> decomposition for the Ni/Ce-La-10Cu-O and Ni/Ce-Sm-10Cu-O catalysts, respectively.

Transient CH<sub>4</sub> and CO decomposition experiments suggested that CH<sub>4</sub> decomposition appears to be the main carbon deposition reaction path in the DRM at 750 °C over the present supported Ni surfaces. In addition, the TOF<sub>CH<sub>4</sub></sub> (s<sup>-1</sup>) of CH<sub>4</sub> decomposition (initial kinetic rate) was found very similar for both La<sup>3+</sup>-based and Sm<sup>3+</sup>-based doped ceria supported Ni surfaces (18 vs 24 nm mean Ni particle size). Different dynamics of carbon deposition and types of carbon (e.g., SCNTs, MWCNTs) formed were observed during CH<sub>4</sub> decomposition (20%CH<sub>4</sub>/He) and CO disproportionation (20%CO/He) reactions at 750 °C (transient kinetic and TPO studies).

#### CRediT authorship contribution statement

**Aseel GS Hussien:** Validation, Investigation. **Constantinos M Damaskinos:** Validation, Investigation. **Aasif A. Dabbawala:** Validation. **Dalaver H. Anjum:** Validation. **Michalis A Vasiliades:**

Validation, Investigation. **Maryam TA Khaleel:** Validation. **Nimer Wehbe:** Validation. **Angelos M Efstatiou:** Methodology, Supervision, Writing – original draft, Revisions. **Kyriaki Polychronopoulou:** Methodology, Supervision, Writing – original draft, Revisions.

#### Declaration of Competing Interest

The authors declare that they have no known competing financial interests or personal relationships that could have appeared to influence the work reported in this paper.

#### Acknowledgements

Aseel Gamal Suliman Hussien and Kyriaki Polychronopoulou acknowledge the financial support from the Abu Dhabi Department of Education and Knowledge (ADEK) through the Abu Dhabi Award Research Excellence (AARE) 2017, grant No. AARE2017-258. Khalifa University is acknowledged for the financial support through the grant RC2-2018-024. The Cyprus Research and Innovation Foundation through the grant INFRASTRUCTURES/1216/0070, and the Research Committee of the University of Cyprus are gratefully acknowledged for the financial support of this work.

#### Appendix A. Supporting information

Supplementary data associated with this article can be found in the online version at doi:10.1016/j.apcatb.2021.121015.

#### References

- [1] M.M. Zain, A.R. Mohamed, An overview on conversion technologies to produce value added products from CH<sub>4</sub> and CO<sub>2</sub> as major biogas constituents, Renew. Sust. Energy Rev. 98 (2018) 56–63.
- [2] C. Papadopoulou, H. Matralis, X. Verykios, Utilization of biogas as a renewable carbon source: dry reforming of methane, in: L. Guczi, A. Erdohelyi (Eds.), Catalysts for Alternative Energy Generation, Springer New York, NY, 2012, pp. 57–127.
- [3] J.A. Martens, A. Bogaerts, N. De Kimpe, P.A. Jacobs, G.B. Marin, K. Rabaey, M. Saeyns, S. Verhelst, Review – the chemical route to a carbon dioxide neutral world, ChemSusChem 10 (2017) 1039–1055.
- [4] Y. Wang, Q. Xia, Fischer-Tropsch synthesis steps into the solar era: lower olefins from syngas, Chem 4 (2018) 2741–2743.
- [5] H. Jahangiri, J. Bennett, P. Mahjoubi, K. Wilson, S. Gu, A review of advanced catalyst development for Fischer-Tropsch synthesis of hydrocarbons from biomass derived syn-gas, Catal. Sci. Technol. 4 (2014) 2210–2229.
- [6] R. Rauch, A. Kiennemann, A. Sauciu, Fischer-Tropsch synthesis to biofuels (BtL process), in: The Role of Catalysis for the Sustainable Production of Bio-fuels and Bio-chemicals, Elsevier, 2013, pp. 397–443.
- [7] H. Mahmoudi, M. Mahmoudi, O. Doustdar, H. Jahangiri, A. Tsolakis, S. Gu, M. LechWyszynski, A review of Fischer Tropsch synthesis process, mechanism, surface chemistry and catalyst formulation, Biofuels Eng. 2 (2018) 11–31.
- [8] T. Kuramochi, A. Ramirez, W. Turkenburg, A. Faaij, Comparative assessment of CO<sub>2</sub> capture technologies for carbon-intensive industrial processes, Prog. Energy Combust. Sci. 38 (2012) 87–112.
- [9] W. Gao, S. Liang, R. Wang, Q. Jiang, Y. Zhang, Q. Zheng, B. Xie, C.Y. Toe, X. Zhu, J. Wang, L. Huang, Y. Gao, Z. Wang, C. Jo, Q. Wang, L. Wang, Y. Liu, B. Louis, J. Scott, A.-C. Roger, R. Amal, H. He, S.-E. Park, Industrial carbon dioxide capture and utilization: state of the art and future challenges, Chem. Soc. Rev. 49 (2020) 8584–8686.
- [10] M. Bui, C.S. Adjiman, A. Bardow, E.J. Anthony, A. Boston, S. Brown, P.S. Fennell, S. Fuss, A. Galindo, L.A. Hackett, J.P. Hallett, J.H. Herzog, G. Jackson, J. Kemper, S. Krevor, G.C. Maitland, M. Matuszewski, I.S. Metcalfe, C. Petit, G. Puxty, J. Reimer, D.M. Reiner, E.S. Rubin, S.A. Scott, N. Shah, B. Smit, J.P.M. Trusler, P. Webley, J. Wilcox, N. Mac Dowell, Carbon capture and storage (CCS): the way forward, Energy Environ. Sci. 11 (2018) 1062–1176.
- [11] D. Pakhare, J. Spivey, A review of dry (CO<sub>2</sub>) reforming of methane over noble metal catalysts, Chem. Soc. Rev. 43 (2014) 7813–7837.
- [12] J.J. Spivey, Fuel cells: technologies for fuel processing, in: D. Shekhawat, J. Spivey, D.A. Berry (Eds.), Deactivation of Reforming Catalysts, Elsevier, 2011.
- [13] J.M. Ginsburg, J. Piña, T. El Solh, H.I. De, Lasa, coke formation over a nickel catalyst under methane dry reforming conditions: thermodynamic and kinetic models, Ind. Eng. Chem. Res. 44 (2005) 4846–4854.
- [14] G. Zhang, J. Liu, Y. Xu, Y. Sun, A review of CH<sub>4</sub>-CO<sub>2</sub> reforming to synthesis gas over Ni-based catalysts in recent years (2010–2017), Int. J. Hydrog. Energy 43 (2018) 15030–15054.

[15] M.A. Vasiliades, P. Djinović, L.F. Davlyatova, A. Pintar, A.M. Efsthathiou, Origin and reactivity of active and inactive carbon formed during DRM over  $\text{Ni}/\text{Ce}_{0.35}\text{Zr}_{0.62}\text{O}_{2-\delta}$  studied by transient isotopic techniques, *Catal. Today* 299 (2018) 201–211.

[16] M.M. Makri, M.A. Vasiliades, K.C. Petallidou, A.M. Efsthathiou, Effect of support composition on the origin and reactivity of carbon formed during dry reforming of methane over 5 wt%  $\text{Ni}/\text{Ce}_{1-x}\text{M}_x\text{O}_{2-\delta}$  ( $\text{M} = \text{Zr}^{4+}, \text{Pr}^{3+}$ ) catalysts, *Catal. Today* 259 (2016) 150–164.

[17] M.A. Vasiliades, P. Djinović, A. Pintar, J. Kovač, A.M. Efsthathiou, The effect of  $\text{CeO}_2$ – $\text{ZrO}_2$  structural differences on the origin and reactivity of carbon formed during methane dry reforming over  $\text{Ni}/\text{CeO}_2$ – $\text{ZrO}_2$  catalysts studied by transient techniques, *Catal. Sci. Technol.* 7 (2017) 5422–5434.

[18] M.A. Vasiliades, C.M. Damaskinos, P. Djinović, A. Pintar, A.M. Efsthathiou, Dry reforming of  $\text{CH}_4$  over  $\text{Ni}/\text{Ce}_{0.75}\text{Zr}_{0.25}\text{O}_{2-\delta}$ : the effect of Co on the site activity and carbon pathways studied by transient techniques, *Catal. Commun.* 149 (2021), 106237.

[19] C.M. Damaskinos, M.A. Vasiliades, A.M. Efsthathiou, The effect of  $\text{Ti}^{4+}$  dopant in the 5 wt%  $\text{Ni}/\text{Ce}_{1-x}\text{Ti}_x\text{O}_{2-\delta}$  catalyst on the carbon pathways of dry reforming of methane studied by various transient and isotopic techniques, *Appl. Catal. A Gen.* 579 (2019) 116–129.

[20] M.A. Vasiliades, C.M. Damaskinos, K.K. Kyprianou, M. Kollia, A.M. Efsthathiou, The effect of Pt on the carbon pathways in the dry reforming of methane over  $\text{Ni}/\text{Pt}/\text{Ce}_{0.8}\text{Pr}_{0.2}\text{O}_{2-\delta}$  catalyst, *Catal. Today* 355 (2020) 788–803.

[21] C.M. Damaskinos, J. Zavánsk, P. Djinovic, A.M. Efsthathiou, Dry reforming of methane over  $\text{Ni}/\text{Ce}_{0.8}\text{Ti}_{0.2}\text{O}_{2-\delta}$ : the effect of Ni particle size on the carbon pathways studied by transient and isotopic techniques, *Appl. Catal. B Environ.* 296 (2021), 120321.

[22] M.A. Vasiliades, M.M. Makri, P. Djinović, B. Erjavec, A. Pintar, A.M. Efsthathiou, Dry reforming of methane over 5 wt%  $\text{Ni}/\text{Ce}_{1-x}\text{Pr}_x\text{O}_{2-\delta}$  catalysts: performance and characterization of active and inactive carbon by transient isotopic techniques, *Appl. Catal. B Environ.* 197 (2016) 168–183.

[23] N.A.K. Aramouni, J.G. Touma, B.A. Tarboush, J. Zeaiter, M.N. Ahmad, Catalyst design for dry reforming of methane: analysis review, *Renew. Sustain. Energy Rev.* 82 (2018) 2570–2585.

[24] I. Luisetto, S. Tuti, C. Romano, M. Boaro, E. Di Bartolomeo, J.K. Kesavan, S. S. Kumar, K. Selvakumar, Dry reforming of methane over Ni supported on doped  $\text{CeO}_2$ : new insight on the role of dopants for  $\text{CO}_2$  activation, *J. CO<sub>2</sub> Util.* 30 (2019) 63–78.

[25] A. Khan, T. Sukonket, B. Saha, R. Idem, Catalytic activity of various 5 wt%  $\text{Ni}/\text{Ce}_{0.5}\text{Zr}_{0.33}\text{M}_{0.17}\text{O}_2$  catalysts for the  $\text{CO}_2$  reforming of  $\text{CH}_4$  in the presence and absence of steam, *Energy Fuel* 26 (2012) 365–379.

[26] S. Das, A. Jangam, S. Jayaprakash, S. Xi, K. Hidajat, K. Tomishige, S. Kawi, Role of lattice oxygen in methane activation on Ni-phyllosilicate@ $\text{Ce}_{1-x}\text{Zr}_x\text{O}_2$  core-shell catalyst for methane dry reforming: Zr doping effect, mechanism, and kinetic study, *Appl. Catal. B Environ.* 290 (2021), 119998.

[27] T. Montini, M. Melchionna, M. Monai, P. Fornasiero, Fundamentals and catalytic applications of  $\text{CeO}_2$ -based materials, *Chem. Rev.* 116 (2016) 5987–6041.

[28] H.A. Lara-García, D.G. Araiza, M. Méndez-Galván, S. Tehuacanero-Cuapa, A. Gómez Cortés, G. Díaz, Dry reforming of methane over nickel supported on Nd- $\text{CeO}_2$ : enhancement of the catalytic properties and coke resistance, *RSC Adv.* 10 (2020) 33059–33070.

[29] C.M. Damaskinos, M.A. Vasiliades, V.N. Stathopoulos, A.M. Efsthathiou, The effect of  $\text{CeO}_2$  preparation method on the carbon pathways in the dry reforming of methane on  $\text{Ni}/\text{CeO}_2$  studied by transient techniques, *Catalysts* 9 (2019) 621–642.

[30] C. Andriopoulou, A. Trimpalis, K.C. Petallidou, A. Sgoura, A.M. Efsthathiou, S. Boghosian, Structural and redox properties of  $\text{Ce}_{1-x}\text{Zr}_x\text{O}_{2-\delta}$  and  $\text{Ce}_{0.8}\text{Zr}_{0.15}\text{RE}_{0.05}\text{O}_{2-\delta}$  (RE: La, Nd, Pr, Y) solids studied by high temperature in situ raman spectroscopy, *J. Phys. Chem. C* 121 (2017) 7931–7943.

[31] M. Yashima, T. Takizawa, Atomic displacement parameters of ceria doped with rare-earth oxide  $\text{Ce}_{0.8}\text{R}_{0.2}\text{O}_{1.9}$  (R= La, Nd, Sm, Gd, Y, and Yb) and correlation with oxide-ion conductivity, *J. Phys. Chem. C* 114 (2010) 2385–2392.

[32] S. Bernal, G. Blanco, A. El Amarti, G. Cifredo, L. Fitian, A. Galtayries, J. Martin, J. M. Pintado, Surface basicity of ceria-supported lanthanum: influence of the calcination temperature, *Surf. Interface Anal.* 38 (2006) 229–233.

[33] K. Polychronopoulou, K. Giannakopoulos, A.M. Efsthathiou, Tailoring  $\text{MgO}$ -based supported Rh catalysts for purification of gas streams from phenol, *Appl. Catal. B Environ.* 111 (2012) 360–375.

[34] A. Kambolis, H. Matralis, A. Trovarelli, C. Papadopoulou,  $\text{Ni}/\text{CeO}_2$ – $\text{ZrO}_2$  catalysts for the dry reforming of methane, *Appl. Catal. A Gen.* 377 (2010) 16–26.

[35] P. Kumar, Y. Sun, R.O. Idem, Nickel-based ceria, zirconia, and ceria-zirconia catalytic systems for low-temperature carbon dioxide reforming of methane, *Energy Fuels* 21 (2007) 3113–3123.

[36] A. Wolfbeisser, O. Sophiphun, J. Bernardi, J. Wittayakun, K. Föttinger, G. Rupprechter, Methane dry reforming over ceria-zirconia supported Ni catalysts, *Catal. Today* 277 (2016) 234–245.

[37] L. Pino, C. Italiano, A. Vita, M. Laganà, V. Recupero,  $\text{Ce}_{0.7}\text{La}_{0.2}\text{Ni}_{0.1}\text{O}_{2-\delta}$  catalyst for methane dry reforming: influence of reduction temperature on the catalytic activity and stability, *Appl. Catal. B Environ.* 218 (2017) 779–792.

[38] K. Polychronopoulou, A.F. Zedan, M. AlKetbi, S. Stephen, M. Ather, M.S. Katsiotis, J. Arvanitidis, D. Christofilos, A.F. Isakovic, S. AlHassan, Tailoring the efficiency of an active catalyst for CO abatement through oxidation reaction: the case study of samarium-doped ceria, *J. Environ. Chem. Eng.* 6 (2018) 266–280 (and references therein).

[39] K. Polychronopoulou, N. Charisiou, K. Papageridis, V. Sebastian, S. Hinder, A. Dabbawala, A. AlKhoori, M. Baker, M. Goula, The effect of Ni addition onto a Cu-based ternary support on the  $\text{H}_2$  production over glycerol steam reforming reaction, *Nanomaterials* 8 (11) (2018) 931 (and references therein).

[40] M. AlKetbi, K. Polychronopoulou, M. Abi Jaoude, M.A. Vasiliades, V. Sebastian, S. J. Hinder, M.A. Baker, A.F. Zedan, A.M. Efsthathiou,  $\text{Cu}-\text{Ce}-\text{La}-\text{O}_x$  as efficient CO oxidation catalysts: effect of Cu content, *Appl. Surf. Sci.* 505 (2020), 144474.

[41] A.A. AlKhoori, K. Polychronopoulou, A. Belabbès, M. Abi Jaoude, L.F. Vega, V. Sebastian, S.S. Hinder, M.A. Baker, A.F. Zedan, Cu, Sm Co-doping effect on the CO oxidation activity of  $\text{CeO}_2$ . A combined experimental and density functional study, *Appl. Surf. Sci.* 521 (2020), 146305.

[42] S. Hull, S.T. Norberg, I. Ahmed, S.G. Eriksson, D. Marrocchelli, P.A. Madden, Oxygen vacancy ordering within anion-deficient ceria, *J. Solid State Chem.* 182 (2009) 2815–2821.

[43] Z. Lu, Z. Yang, B. He, C. Castleton, K. Hermansson, Cu-doped ceria: oxygen vacancy formation made easy, *Chem. Phys. Lett.* 510 (2011) 60–66.

[44] X. Wang, J.A. Rodriguez, J.C. Hanson, D. Gamarra, A. Martinez-Arias, M. Fernández García, Unusual physical and chemical properties of Cu in  $\text{Ce}_{1-x}\text{Cu}_x\text{O}_2$  oxides, *J. Phys. Chem. B* 109 (2005) 19595–19603.

[45] Z. Hu, H. Metiu, Effect of dopants on the energy of oxygen-vacancy formation at the surface of ceria: local or global? *J. Phys. Chem. C* 115 (2011) 17898–17909.

[46] T.V. Sagar, D. Padmakar, N. Lingaiah, P.S.S. Prasad, Influence of solid solution formation on the activity of  $\text{CeO}_2$  supported Ni–Cu mixed oxide catalysts in dry reforming of methane, *Catal. Lett.* 149 (2019) 2597–2606.

[47] A. Trovarelli, P. Fornasiero, Catalysis by ceria and related materials, in: G. H. Hutchings (Ed.), *Catalytic Science Series*, vol. 12, Imperial College Press, 2013.

[48] J.X.Y.H. Huanhuan, S.X. Zhang, Effects of preparation methods on the activity of  $\text{CuO}/\text{CeO}_2$  catalysts for CO oxidation, *Front. Chem. Sci. Eng.* 11 (2017) 603–612.

[49] H. Yang, C. Huang, A. Tang, X. Zhang, W. Yang, Microwave-assisted synthesis of ceria nanoparticles, *Mater. Res. Bull.* 40 (2005) 1690–1695.

[50] Q. Chen, W. Cai, Y. Liu, S. Zhang, Y. Li, D. Huang, T. Wang, Y. Li, Synthesis of  $\text{Cu}_{0.8}\text{Zr}_{0.2}\text{O}_2$  catalyst by ball milling for  $\text{CO}_2$  reforming of ethanol, *J. Saudi Chem. Soc.* 23 (2019) 111–117.

[51] S. Rossignol, F. Gérard, D. Duprez, Effect of the preparation method on the properties of zirconia-ceria materials, *J. Mater. Chem.* 9 (1999) 1615–1620.

[52] Y.-J. Zhu, F. Chen, Microwave-assisted preparation of inorganic nanostructures in liquid phase, *Chem. Rev.* 114 (2014) 6462–6555.

[53] M.A. Surati, S. Jauhari, K.R. Desai, A brief review: microwave assisted organic reaction, *Arch. Appl. Sci. Res.* 4 (2012) 645–661.

[54] J.R.H. Ross, Catalyst characterization, *Contemporary Catalysis*, Elsevier, 2019, pp. 121–132.

[55] S. Brunauer, P.H. Emmett, E. Teller, Adsorption of gases in multimolecular layers, *J. Am. Chem. Soc.* 60 (1938) 309–319.

[56] E.P. Barrett, L.G. Joyner, P.P. Halenda, The determination of pore volume and area distributions in porous substances. I. computations from nitrogen isotherms, *J. Am. Chem. Soc.* 73 (1951) 373–380.

[57] K. Polychronopoulou, C.N. Costa, A.M. Efsthathiou, The steam reforming of phenol reaction over supported-Rh catalysts, *Appl. Catal. A Gen.* 272 (2004) 37–52.

[58] M.A. Vasiliades, D. Harris, H. Stephenson, S. Boghosian, A.M. Efsthathiou, A novel analysis of transient isothermal  $^{18}\text{O}$  isotopic exchange on commercial  $\text{Ce}_x\text{Zr}_{1-x}\text{O}_{2-\delta}$ -based OSC materials, *Top. Catal.* 62 (2019) 219–226.

[59] G.A.O. Meiyi, N. Jiang, Z. Yuhong, X.U. Changjin, S.U. Haiquan, Z. Shanghong, Copper cerium oxides supported on carbon nanomaterial for preferential oxidation of carbon monoxide, *J. Rare Earths* 34 (2016) 55–60.

[60] K. Kuntaiah, P. Sudarsanam, B.M. Reddy, A. Vinu, Nanocrystalline  $\text{Ce}_{1-x}\text{Sm}_x\text{O}_{2-\delta}$  ( $x=0.4$ ) solid solutions: structural characterization versus CO oxidation, *RSC Adv.* 3 (2013) 7953–7962.

[61] D.R. Ou, T. Mori, F. Ye, T. Kobayashi, J. Zou, G. Auchterlonie, J. Drennan, Oxygen vacancy ordering in heavily rare-earth-doped ceria, *Appl. Phys. Lett.* 89 (2006), 171911.

[62] L.H. Reddy, G.K. Reddy, D. Devaiah, B.M. Reddy, A rapid microwave-assisted solution combustion synthesis of  $\text{CuO}$  promoted  $\text{CeO}_2$ – $\text{M}_x\text{O}_y$  ( $\text{M}=\text{Zr, La, Pr and Sm}$ ) catalysts for CO oxidation, *Appl. Catal. A Gen.* 445 (2012) 297–305.

[63] M.D. Donohue, G.L. Aranovich, Classification of Gibbs adsorption isotherms, *Adv. Colloid Interface Sci.* 76 (1998) 137–152.

[64] A. Gurbani, J.L. Ayastuy, M.P. González-Marcos, M.A. Gutiérrez-Ortiz,  $\text{CuO}/\text{CeO}_2$  catalysts synthesized by various methods: comparative study of redox properties, *Int. J. Hydrog. Energy* 35 (2010) 11582–11590.

[65] T. Mori, J. Drennan, J.-H. Lee, J.-G. Li, T. Ikegami, Oxide ionic conductivity and microstructures of Sm- or La-doped  $\text{CeO}_2$ -based systems, *Solid State Ion.* 154 (2002) 461–466.

[66] D.R. Ou, T. Mori, F. Ye, M. Takahashi, J. Zou, J. Drennan, Microstructures and electrolytic properties of yttrium-doped ceria electrolytes: dopant concentration and grain size dependences, *Acta Mater.* 54 (2006) 3737–3746.

[67] D. Su, M. Ford, G. Wang, Mesoporous NiO crystals with dominantly exposed {110} reactive facets for ultrafast lithium storage, *Sci. Rep.* 2 (2012) 924.

[68] P. Li, J. Liu, N. Nag, P.A. Crozier, In situ preparation of Ni–Cu/TiO<sub>2</sub> bimetallic catalysts, *J. Catal.* 262 (2009) 73–82.

[69] A.R. Naghash, T.H. Etsell, S. Xu, XRD and XPS study of Cu–Ni interactions on reduced copper–nickel–aluminum oxide solid solution catalysts, *Chem. Mater.* 18 (2006) 2480–2488.

[70] D.R. Mullins, The surface science of cerium oxide, *Chem. Sci. Div. Oak Ridge Nat. Lab.* (2008).

[71] A. Trovarelli, *Catalysis by Ceria and Related Materials*, World Scientific, 2002.

[72] J.W. Cho, S.J. Park, W. Kim, B.K. Min, Fabrication of nanocrystal ink based superstrate-type  $\text{CuInS}_2$  thin film solar cells, *Nanotechnology* 23 (2012), 265401.

[73] M.C.M. Higgins, J.V. Rojas, Growth kinetics of lanthanum phosphate core/shell, *Process. Prop. Des. Adv. Ceram. Compos.* (2016) 45.

[74] D. Loche, L.M. Morgan, A. Casu, G. Mountjoy, C. O'Regan, A. Corrias, A. Falqui, Determining the maximum lanthanum incorporation in the fluorite structure of La-doped ceria nanocubes for enhanced redox ability, *RSC Adv.* 9 (2019) 6745–6751.

[75] H. Yahirō, Y. Eguchi, K. Eguchi, H. Arai, Oxygen ion conductivity of the ceria-samarium oxide system with fluorite structure, *J. Appl. Electrochem.* 18 (1988) 527–531.

[76] G. Basina, K. Polychronopoulou, A.F. Zedan, K. Dimos, M.S. Katsiotis, A. P. Fotopoulos, I. Ismail, V. Tzitzios, Ultrasmall metal-doped CeO<sub>2</sub> nanoparticles for low-temperature CO oxidation, *ACS Appl. Nano Mater.* 3 (2020) 10805–10813.

[77] E. Meloni, M. Martino, V. Palma, A short review on Ni based catalysts and related engineering issues for methane steam reforming, *Catalysts* 10 (3) (2020) 352.

[78] A.V. Fedorov, R.G. Kukushkin, P.M. Yeletsky, O.A. Bulavchenko, Y.A. Chesarov, V. A. Yakovlev, Temperature-programmed reduction of model CuO, NiO and mixed CuO–NiO catalysts with hydrogen, *J. Alloy. Compd.* 844 (2020), 156135.

[79] V.V. Thyssen, T.A. Maia, E.M. Assaf, Cu, Ni catalysts supported on  $\gamma$ -Al<sub>2</sub>O<sub>3</sub> and SiO<sub>2</sub> assessed in glycerol steam reforming reaction, *J. Braz. Chem. Soc.* 26 (2014) 22e31.

[80] F. Yang, J. Wei, W. Liu, J. Guo, Y. Yang, Copper doped ceria nanospheres: surface defects promoted catalytic activity and a versatile approach, *J. Mater. Chem. A* 2 (2014) 5662–5667.

[81] A.R. Ardiyanti, M.V. Bykova, S.A. Khromova, W. Yin, R.H. Venderbosch, V. A. Yakovlev, H.J. Heeres, Ni-based catalysts for the hydrotreatment of fast pyrolysis oil, *Energy Fuels* 30 (2016) 1544–1554.

[82] Y. She, Q. Zheng, L. Li, Y. Zhan, C. Chen, Y. Zheng, X. Lin, Rare earth oxide modified CuO/CeO<sub>2</sub> catalysts for the water–gas shift reaction, *Int. J. Hydrog. Energy* 34 (2009) 8929–8936.

[83] P. Kumar, V.C. Srivastava, I.M. Mishra, Synthesis and characterization of Ce–La oxides for the formation of dimethyl carbonate by transesterification of propylene carbonate, *Catal. Commun.* 60 (2015) 27–31.

[84] K.R. Hahn, M. Iannuzzi, A.P. Seitsonen, J. Hutter, Coverage effect of the CO<sub>2</sub> adsorption mechanisms on CeO<sub>2</sub>(111) by first principles analysis, *J. Phys. Chem. C* 117 (2013) 1701–1711.

[85] R. Dębek, M. Motak, M.E. Galvez, T. Grzybek, P. Da Costa, Influence of Ce/Zr molar ratio on catalytic performance of hydrotalcite-derived catalysts at low temperature CO<sub>2</sub> methane reforming, *Int. J. Hydrog. Energy* 42 (2017) 23556–23567.

[86] M.A.A. Aziz, A.A. Jalil, S. Wongsakulphasatch, D.-V.N. Vo, Understanding the role of surface basic sites of catalysts in CO<sub>2</sub> activation in dry reforming of methane: a short review, *Catal. Sci. Technol.* 10 (2020) 35–45.

[87] V.R. Bach, A.C. de Camargo, T.L. de Souza, L. Cardozo-Filho, H.J. Alves, Dry reforming of methane over Ni/MgO-Al<sub>2</sub>O<sub>3</sub> catalyst: Thermodynamic equilibrium analysis and experimental applications, *Int. J. Hydrog. Energy* 45 (2020) 5252–5263.

[88] L.R. Radovic, Active sites in graphene and the mechanism of CO<sub>2</sub> formation in carbon oxidation, *J. Am. Chem. Soc.* 131 (2009) 17166–17175.

[89] A. Chatla, M.M. Ghouri, O.W. El Hassan, N. Mohamed, A.V. Prakash, N.O. Elbashir, An experimental and first principles DFT investigation on the effect of Cu addition to Ni/Al<sub>2</sub>O<sub>3</sub> catalyst for the dry reforming of methane, *Appl. Catal. A Gen.* 602 (2020), 117699.

[90] K. Song, M. Lu, S. Xu, C. Chen, Y. Zhan, D. Li, C. Au, L. Jiang, K. Tomishige, Effect of alloy composition on catalytic performance and coke-resistance property of Ni/Cu/Mg(Al)O catalysts for dry reforming of methane, *Appl. Catal. B Environ.* 239 (2018) 324–333.

[91] J.F. Tu, TEM nano-moiré pattern analysis of a copper/single walled carbon nanotube nanocomposite synthesized by laser surface implanting, *C. J. Carbon Res* 4 (2018) 19.

[92] F. Yu, W. Zhou, Alloying and dealloying of CuPt bimetallic nanocrystals, *Prog. Nat. Sci. Mater. Int.* 23 (2013) 331–337.

[93] W. Zhou, Z. Han, J. Wang, Y. Zhang, Z. Jin, X. Sun, Y. Zhang, C. Yan, Y. Li, Copper catalyzing growth of single-walled carbon nanotubes on substrates, *Nano Lett.* 6 (2006) 2987–2990.

[94] T. Manoubi, M. Tencé, C. Colliex, Quantification of white lines in electron energy loss spectroscopy (EELS), *Ultramicroscopy* 28 (1989) 49–55.

[95] R.F. Egerton, *Electron Energy-loss Spectroscopy in the Electron Microscope*, Springer, 2011.

[96] I. Luisetto, S. Tuti, E. Di Bartolomeo, Co and Ni supported on CeO<sub>2</sub> as selective bimetallic catalyst for dry reforming of methane, *Int. J. Hydrog. Energy* 37 (2012) 15992–15999.

[97] B.E. Al-Sabban, Development of Coke-tolerant Transition Metal Catalysts for Dry Reforming of Methane (Ph.D. thesis), King Abdullah University of Science and Technology, 2016.

[98] W.-J. Jang, D.-W. Jeong, J.-O. Shim, H.-M. Kim, W.-B. Han, J.-W. Bae, H.-S. Roh, Metal oxide (MgO, CaO and La<sub>2</sub>O<sub>3</sub>) promoted Ni-Ce<sub>0.8</sub>Zr<sub>0.2</sub>O<sub>2</sub> catalysts for H<sub>2</sub> and CO production from two major greenhouse gases, *Renew. Energy* 79 (2015) 91–95.